

# A quantitative comparison of high latitude electric field models during a large geomagnetic storm

Lauren Orr<sup>1</sup>, Adrian Grocott<sup>2</sup>, Maria-Theresia Walach<sup>2</sup>, Gareth Chisham<sup>3</sup>, Mervyn P. Freeman<sup>3</sup>, Mai Mai Lam<sup>3</sup>, and Robert Michael Shore<sup>3</sup>

<sup>1</sup>British Geological Survey

<sup>2</sup>Lancaster University

<sup>3</sup>British Antarctic Survey

January 20, 2023

## Abstract

Models of the high-latitude ionospheric electric field are commonly used to specify the magnetospheric forcing in thermosphere or whole atmosphere models. The use of decades-old models based on spacecraft data is still widespread. Currently the Heelis and Weimer climatology models are most commonly used but it is possible a more recent electric field model could improve forecasting functionality. Modern electric field models, derived from radar data, have been developed to incorporate advances in data availability. It is expected that climatologies based on this larger and up-to-date dataset will better represent the high latitude ionosphere and improve forecasting abilities. An example of two such models, which have been developed using line-of-sight velocity measurements from the Super Dual Auroral Radar Network (SuperDARN) are the Thomas and Shepherd model (TS18), and the Time-Variable Ionospheric Electric Field model (TiVIE). Here we compare the outputs of these electric field models during the September 2017 storm, covering a range of solar wind and interplanetary magnetic field (IMF) conditions. We explore the relationships between the IMF conditions and the model output parameters such as transpolar voltage, the polar cap size and the lower latitude boundary of convection. We find that the electric potential and field parameters from the spacecraft-based models have a significantly higher magnitude than the SuperDARN-based models. We discuss the similarities and differences in topology and magnitude for each model.

1 **A quantitative comparison of high latitude electric field**  
2 **models during a large geomagnetic storm**

3 **L. Orr<sup>1,3</sup>, A. Grocott<sup>1</sup>, M.-T. Walach<sup>1</sup>, G. Chisham<sup>2</sup>, M.P. Freeman<sup>2</sup>, M.M.**  
4 **Lam<sup>2</sup>, R.M. Shore<sup>2</sup>**

5 <sup>1</sup>Space and Planetary Physics, Lancaster University

6 <sup>2</sup>British Antarctic Survey

7 <sup>3</sup>Now at British Geological Survey

8 **Key Points:**

- 9
- 10 • The Heelis model is hugely dependent on the transpolar voltage proxy used as in-  
11 put and when based on the Kp index it is very poor
  - 12 • Models similar during quiet conditions but the spacecraft-based models are vastly  
13 different to the SuperDARN-based models during storm times
  - 14 • As storm times are important for Joule Heating and satellite drag these differences  
must be considered by model users

**Abstract**

Models of the high-latitude ionospheric electric field are commonly used to specify the magnetospheric forcing in thermosphere or whole atmosphere models. The use of decades-old models based on spacecraft data is still widespread. Currently the Heelis (Heelis et al., 1982) and Weimer (Weimer, 2005) climatology models are most commonly used but it is possible a more recent electric field model could improve forecasting functionality. Modern electric field models, derived from radar data, have been developed to incorporate advances in data availability (Thomas & Shepherd, 2018; Walach et al., 2022; Bristow et al., 2022). It is expected that climatologies based on this larger and up-to-date dataset will better represent the high latitude ionosphere and improve forecasting abilities. An example of two such models, which have been developed using line-of-sight velocity measurements from the Super Dual Auroral Radar Network (SuperDARN) are the Thomas and Shepherd model (TS18) (Thomas & Shepherd, 2018), and the Time-VARIABLE Ionospheric Electric Field model (TiVIE) (Walach & Grocott, 2022). Here we compare the outputs of these electric field models during the September 2017 storm, covering a range of solar wind and interplanetary magnetic field (IMF) conditions. We explore the relationships between the IMF conditions and the model output parameters such as transpolar voltage, the polar cap size and the lower latitude boundary of convection. We find that the electric potential and field parameters from the spacecraft-based models have a significantly higher magnitude than the SuperDARN-based models. We discuss the similarities and differences in topology and magnitude for each model.

**Plain Language Summary**

To prevent collisions between satellites and space junk within the Earth’s space environment we need to accurately predict their position. The Ionosphere is part of the upper atmosphere of the Earth which is affected by space weather events such as geomagnetic storms. Accurate ionospheric electric field models are key to accurate orbit prediction. Currently the use of decades-old models based on spacecraft data from the 80s is still widespread. We aim to compare the output from these commonly used spacecraft-based models to more recent models which were developed using line-of-sight velocity measurements from the Super Dual Auroral Radar Network (SuperDARN). We find that the parameters output from the spacecraft-based models often are significantly different to the SuperDARN-based models. We discuss the similarities and differences in topology and magnitude for each model.

**1 Introduction**

The high latitude ionospheric electric field is driven by coupling of the solar wind, magnetosphere and ionosphere. It is an integral part of space weather and can affect both ground-based and space-born technology; it is therefore important that we can accurately model the ionospheric electric field. For example, the ionospheric electric field is an important source of uncertainty in satellite drag and hence the risk of collisions between satellites and space debris. The electric field causes ions and electrons to accelerate parallel to the electric field and drift perpendicular to it such that they collide with neutral particles and heat the thermosphere. This Joule heating expands the thermosphere, causing the air density to locally increase and hence satellite drag.

One impact of the Space Weather Instrumentation, Measurement, Modelling and Risk: Thermosphere (SWIMMR-T) programme aims to improve the UK’s ability to specify and forecast the thermosphere. To do this, it is using and developing a physics-based, coupled thermosphere-ionosphere assimilative model for satellite drag and other applications called AENeAS (Advanced Ensemble electron density [Ne] Assimilation System) (Elvidge & Angling, 2019). AENeAS is based on the Thermosphere Ionosphere Electrodynamics General Circulation Model (TIEGCM (Dickinson et al., 1981)) which requires

an appropriate ionospheric electric field model of which there are many models currently used routinely in space physics. Heelis et al. (1982) and Weimer (2005) are two climatological models based on spacecraft data that are commonly used in modern atmospheric and space weather models. Currently TIEGCM and hence AENeAS interchangeably uses either a version of the Heelis et al. (1982) model, similar to that from M. Hairston and Heelis (1990), or the Weimer (2005) model but it is possible that a ‘state-of-the-art’ electric field model will improve its functionality. Similarly, the Whole Atmosphere Community Climate Model With Thermosphere and Ionosphere Extension (WACCM-X) (Liu et al., 2018), is another General Circulation Model (GCM) which currently uses Heelis to specify the electric field patterns, but Liu et al. (2018) suggests that the use of Weimer (2005) or data assimilative schemes (Richmond & Kamide, 1988) would improve its simulations.

The Super Dual Auroral Radar Network (SuperDARN) (Chisham et al., 2007), a collection of ground-based coherent scatter radars, has been used for many years to measure and model ionospheric convection (Ruohoniemi & Baker, 1998). The addition of SuperDARN-based models could potentially help improve TIEGCM, AENeAS, WACCM-X and other modern GCMs by having an ionosphere model based on a spatially and temporally well sampled dataset from the most recent solar cycle.

Table 1 summarises the Heelis, Weimer, and SuperDARN family of models and highlights the similarities and differences between them. An important difference is the time interval of data on which each model is based, which is illustrated in Figure 1 in relation to the solar cycle and sunspot number. Figure 1 plots the previous four solar cycles (SC21-24) with shading showing the time range over which each of the models were devised. Weimer (2005) and M. Hairston and Heelis (1990), denoted W05 and HH90 respectively, cover the 20 month period in the declining phase of SC21 for which Dynamics Explorer 2 (DE-2) was active. Ruohoniemi and Greenwald (1996) (RG96) covered most of SC22, Pettigrew et al. (2010) (PSR10) most of of SC23, Cousins and Shepherd (2010) (CS10) the majority of SC23 and Thomas and Shepherd (2018) (TS18) and Walach and Grocott (2022) (TiVIE) most of SC24.

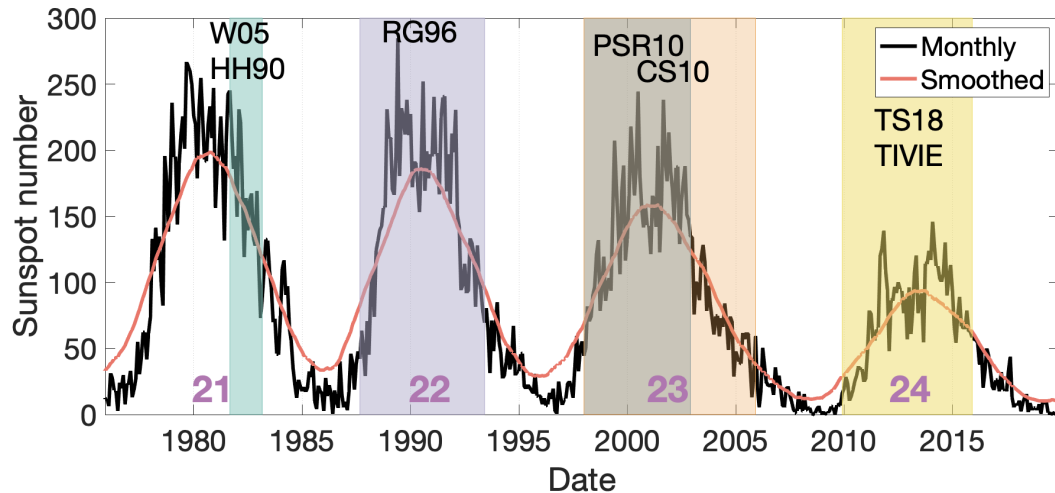


**Figure 1.** Monthly mean total sunspot number with W05, HH90, RG96, PSR10, CS10 and TS18 time spans.

Heelis et al. (1982) was originally a purely mathematical model for high latitude ionospheric convection based on Volland (1975). This model takes input parameters such

96 as the radius of the convection reversal boundary, the longitude of the dayside and night-  
 97 side zero potential lines, and the magnitude of the maximum and minimum electric po-  
 98 tentials. The full list of input variables are specified in section 1, Supplementary Infor-  
 99 mation (SI).

100 This model was further developed by M. Hairston and Heelis (1990) such that the  
 101 convection pattern was parameterised by the Interplanetary Magnetic Field (IMF)  $B_y$   
 102 and the transpolar voltage,  $\Phi_{PC}$ , only. They used data from DE-2, which operated be-  
 103 tween August 1981 and March 1983 in a polar orbit at altitudes of 300-1000km, to find  
 104 relationships between the parameters in Heelis et al. (1982) with  $B_y$  and  $\Phi_{PC}$ . The DE-  
 105 2 passes used in this analysis were limited to those starting and ending within 3 hours  
 106 of magnetic local time (MLT) of the dawn-dusk meridian during intervals with IMF  $B_z$   
 107 negative. Fewer than 100 passes fulfilled those criteria.

ID	Reference	Time span	Solar cycle	Data source	Para- meters	Grid	Lower bound- ary
H82	Heelis 1982				See tbl. S1, SI	Analytical.	Equator.
HH90	Hairston & Heelis 1990	08/1981 - 03/1983 (< 100 passes)	SC21 (max. - declining phase)	DE-2	$\Phi_{PC}$ , $B_y$ , $-B_z$ only	Analytical, contin- uous, offset polar cap	Equator.
W05	Weimer 2005	08/1981 - 03/1983 (2064 passes)	SC21 (max. - declining phase)	DE-2	$B_y$ , $B_z$ , $n$ , $V$ , tilt	Define $N$ bands of width $D = \frac{R}{60}$ . For radius $\frac{R}{D} \leq 26$ , do SH cap fit. For $26 < \frac{R}{D} \leq 60$ , do azimuthal Fourier expansions per band.	4.2° offset circle with radius $R = f(\theta, B_{yz}, V, n)$ .
TS18	Thomas & Shep- herd 2018	2010- 2016	SC24 (min. - declining phase)	Super- DARN (SD)	$E_{sw}$ , $\theta_{clk}$ , tilt	SH cap fit where cap size is circle whose lowest lati- tude equals HMB.	Min. latitude HMB with max. midnight latitude for merged vectors with $V > 150$ m/s for 25+ points adjacent to boundary.
TS18 Kp	Thomas & Shep- herd 2018	2010- 2016	As above	SD	Kp, $\theta_{clk}$	As above	As above
TiVIE (mode 3)	Walach et al 2022	54 storms 2010- 2016	As above	SD	Storm Phase: Sym-H	As above	The lower quar- tile (25%) of the HMBs from the original maps is used.

**Table 1.** List of commonly used electric field models with details summarised.

108 The Weimer model (Weimer, 2005) (W05) is a statistical electric potential model  
 109 of the high-latitude ionosphere. Measurements of the ionospheric electric field from more  
 110 than 2600 passes of the DE-2 satellite were used alongside solar wind and IMF condi-  
 111 tions to create an empirical model of potential patterns. The model was developed from  
 112 measurements of the electric potential variation along the satellite path estimated from  
 113 the integration of electric field components in the direction of motion. This model has  
 114 been updated a number of times to increase spacecraft resolution, with the low-latitude  
 115 boundary varying and improving the representation of the potentials using a combina-  
 116 tion of Fourier series and spherical harmonics (Weimer, 1995, 1996, 2001, 2005). Input  
 117 parameters include the IMF  $B_y$  and  $B_z$  components, the dipole tilt angle of the Earth,  
 118 the solar wind velocity  $V$ , and the plasma number density  $n$ . Electric potential is cal-  
 119 culated at different points in geomagnetic latitude and magnetic local time (MLT), in  
 120 AACGM (Altitude Adjusted Corrected Geomagnetic) coordinates. Weimer (2005) de-  
 121 fines 60 latitude bands then uses spherical harmonics to describe the potentials within  
 122 the highest 26 bands around the offset pole. Fourier series as a function of angular po-  
 123 sition (and parameters) are used to represent the potentials in the lower 34 latitude bands.

124 Ruohoniemi and Greenwald (1996) were first to use line-of-sight  $E \times B$  velocity  
 125 measurements from SuperDARN to derive a set of statistical electric potential patterns  
 126 organized by IMF magnitude and clock angle. This ‘climatological’ model was primar-  
 127 ily built to augment instantaneous SuperDARN measurements in the SuperDARN fit-  
 128 ting procedure known as Map Potential (Ruohoniemi & Baker, 1998). Map Potential uses  
 129 all available SuperDARN line-of-sight velocity data at a given time to derive an instan-  
 130 taneous spherical harmonic solution of the electrostatic potential that is constrained by  
 131 the statistical model in regions of no data coverage. Consequently the Map Potential so-  
 132 lution tends towards the instantaneous measured data where it exists and towards the  
 133 climatological model where the measurements are missing. Pettigrew et al. (2010) im-  
 134 proved the climatological model by adding dipole tilt angle as a parameter and Cousins  
 135 and Shepherd (2010) expanded the dataset and added a dependence on solar wind ve-  
 136 locity. Recently Thomas and Shepherd (2018) developed this model further using data  
 137 from solar cycle 24, which exploited the expansion of SuperDARN radars to mid-latitudes  
 138 ( $50-60^\circ$ ) and to the polar cap ( $80-90^\circ$ ). Their climatological electric potential pat-  
 139 terns were organized by the solar wind electric field magnitude ( $E_{sw}$ ), the IMF clock an-  
 140 gle ( $\theta_{clk}$ ), and the dipole tilt angle. This is the model version currently used in Map Po-  
 141 tential. Thomas and Shepherd (2018) further included a version of their climatology pa-  
 142 rameterised by the magnetic planetary ‘Kp’ index and clock angle.

143 A more recent model that can be used to improve ionospheric electric field repre-  
 144 sentation within atmosphere modelling is the Time-Variable Ionospheric Electric field  
 145 (TiVIE) model (Walach & Grocott, 2022). Unlike previous SuperDARN-based models,  
 146 which are based on instantaneous climatologies, TiVIE makes use of novel parameter-  
 147 isations to capture major sources of time-variability in the electric field pattern. TiVIE  
 148 combines SuperDARN data into superposed epoch analyses to model the electric field  
 149 using spherical harmonics for different time-varying scenarios via one of three modes. Mode  
 150 1 is directly related to the upstream solar wind conditions of the IMF, parameterised by  
 151 IMF strength bins, clock angle and a solar wind steadiness timescale. This latter param-  
 152 eter allows for differences in the duration of a given state of solar wind driving to be cap-  
 153 tured. Mode 2 is a substorm mode, and may be parameterised by the universal time, mag-  
 154 netic latitude and local time, of a substorm onset. This allows for variability due to the  
 155 substorm, that may be temporally decoupled from the solar wind driver, to be captured.  
 156 Mode 3 parameterises the electric field by storm phase using Sym-H to account for the  
 157 variability introduced specifically by geomagnetic storms. This mode is based on a list  
 158 of 54 storms from 2010-2016 (Walach & Grocott, 2019; Walach et al., 2021). Geomag-  
 159 netic storms are a major source of variability that is not captured using instantaneous  
 160 IMF parameterisations. Instead of the instantaneous IMF, the mode 3 model uses the  
 161 normalised time within the initial, main, and recovery phases defined using the Sym-H

162 index. SuperDARN measurements at each normalised time are then averaged over all  
 163 storms to estimate the electric potential by a spherical harmonic fit.

164 In this paper we will quantitatively compare the aforementioned ionospheric elec-  
 165 tric field models (HH90, W05, TS18, and TiVIE) for the 7th-8th September 2017 geo-  
 166 magnetic storm. Choosing a storm interval allows us to test the models under extreme  
 167 driving conditions when space weather impacts will be greatest and when we might ex-  
 168 pect the models to be most deficient and diverse due to their limited input dataset. It  
 169 also enables us to contrast models based on typical data with the storm mode of the TiVIE  
 170 model that is specifically tailored to storm times. Although we have chosen a single event,  
 171 the storm we have picked nonetheless encompasses a variety of solar wind driving con-  
 172 ditions and thus a range of input parameterisation to the models, and there is good Su-  
 173 perDARN data coverage throughout the main phase of the storm. Performing an event-  
 174 based comparison, rather than a statistical study avoids the complication introduced by  
 175 the models having different input parameters (see Table 1). For example, TS18 is pa-  
 176 rameterised by solar wind electric field  $E_{sw}$  and clock angle  $\theta_{clk}$ , whereas W05 is param-  
 177 eterised by solar wind speed  $V$  and IMF  $B_y$  and  $B_z$  components. Consequently, the TS18  
 178 and W05 statistical model outputs cannot be uniquely compared because a given  $E_{sw}$   
 179 and  $\theta_{clk}$  state can in general arise from different combinations of  $V$ ,  $B_y$ , and  $B_z$ , whereas  
 180 a given event naturally selects all parameter values. Event-based comparison also allows  
 181 us to compare the model outputs to the SuperDARN Map Potential output as a “ground-  
 182 truth” dataset, recognising that we are comparing this “ground-truth” to both Super-  
 183 DARN and non-SuperDARN models.

184 In section 2 we describe the method, the model versions and the data used, sec-  
 185 tion 3 shows the results and section 4 discusses the findings.

## 186 2 Methods

### 187 2.1 Model versions

188 The models used in this study are summarised in Table 1. The version of the Heelis  
 189 model used for the analysis in this paper is taken from TIEGCM (Qian et al., 2014) within  
 190 AENeAS (Elvidge & Angling, 2019; HAO, 2018). A full description of the code is included  
 191 in the SI but we will refer to it as HH90 due to its similarities with M. Hairston and Heelis  
 192 (1990). The W05 model is described by Weimer (2005) and was provided by Daniel Weimer.  
 193 TS18 (Thomas & Shepherd, 2018) is available as part of the Radar Software Toolkit (RST  
 194 (4.4.1)) (SuperDARN Data Analysis Working Group et al., 2021). TiVIE refers to the  
 195 geomagnetic storm (mode 3) version.

### 196 2.2 Selection of event

197 The chosen interval of interest is from 20:00 UT on September 7th to 03:20 UT on  
 198 September 8th. The interval is within a geomagnetic storm, as shown in Figure 1 of the  
 199 Supplementary Information by the characteristic rapid decrease in the Sym-H index and  
 200 slow recovery. The minimum Sym-H is  $-146$  nT, which defines this event as an intense  
 201 storm ( $-250$  nT < minimum Sym-H <  $-100$  nT).

202 Following the definition of storm phases devised by Walach and Grocott (2019) for  
 203 mode 3 of the TiVIE model, the storm begins at 11:02 UT on 7th September and ends  
 204 at 18:40 UT on 10th September. Within this, the storm’s initial phase is from 11:02 to  
 205 23:07 UT on 7th September, the main phase then follows until 01:08 UT on 8th Septem-  
 206 ber, and thereafter the recovery phase until the storm end at 18:40 UT on 10th Septem-  
 207 ber. It should be noted that the Walach and Grocott (2019) definition of the start of a  
 208 storm is not based on the Sudden Storm Commencement (SSC), as is commonly the case.  
 209 Instead, it is the start of a storm initial phase that is defined as a quiet interval ahead

210 of the storm main phase in which Sym-H maximises and is greater than -15 nT. The Walach  
 211 and Grocott definition is more practical for storms without an SSC or due to the inter-  
 212 action of multiple solar ejecta, as is the case in this storm (Dimmock et al., 2019). The  
 213 7 hour 20 minute interval within the storm has been selected to include the 2 hour 3 minute  
 214 main phase from 23:07 UT (7th) to 01:10 UT (8th) and similar length intervals of the sur-  
 215 rounding initial and recovery phases.

### 216 2.3 Model input control variables

217 As mentioned in the Introduction, the decision to use a single event to compare the  
 218 models is because they each have different control variables as input (see Table 1) which  
 219 cannot be uniquely related to each other. For example, (i) TS18 has 120 climatological  
 220 patterns for different combinations of inputs  $E_{sw}$ ,  $\theta_{clk}$ , and dipole tilt angle (where  $E_{SW} =$   
 221  $|V_x| \sqrt{B_y^2 + B_z^2}$  and  $\theta_{clk} = \arctan(\frac{B_y}{B_z})$ ), (ii) W05 input control variables includes IMF  
 222  $B_y$ ,  $B_z$ , the dipole tilt angle of the Earth, solar wind velocity,  $V$ , and plasma number  
 223 density,  $n$ . (iii) HH90 takes  $\Phi_{PC}$  and IMF  $B_y$  as input control variables, and (iv) TiVIE  
 224 mode 3 uses only storm phase and normalised time within it.

225 Considering first TiVIE mode 3, the ionospheric electric field is defined in this model  
 226 for each time step within the initial, main, and recovery phases at 2 minutes cadence.  
 227 The duration of these phases are defined in the model to be 587, 272, and 1673 time steps,  
 228 respectively, corresponding to the average length in minutes of these phases for the 54  
 229 storms on which the model is based. For the September 2017 storm event studied here,  
 230 the duration of the initial, main and recovery phases are found to be 725, 121, and 3932  
 231 min, respectively. Thus the model time step in each phase is scaled by the ratio of the  
 232 event phase duration to the model phase duration, i.e.,  $725/587 = 1.24$  min,  $121/272 =$   
 233  $0.445$  min, and  $3932/1673 = 2.35$  min for the initial, main, and recovery phases, respec-  
 234 tively. Consequently, for the interval of interest from 20:00 UT on 7 September to 03:20 UT  
 235 on 8 September, we use the final 151 of the 587 time steps of the model initial phase,  
 236 all 272 time steps of the model main phase, and the first 57 of the 1673 time steps of the  
 237 model recovery phase, making a total of 480 model time steps.

238 For the W05 and TS18 models, the interplanetary input control variables are pro-  
 239 vided by, or derived from, measurements from the ACE (Advanced Composition Explorer)  
 240 and WIND spacecraft in the OMNI dataset of the NASA Geophysical Data Center [http://](http://omniweb.gsfc.nasa.gov/ow.html)  
 241 [omniweb.gsfc.nasa.gov/ow.html](http://omniweb.gsfc.nasa.gov/ow.html). The measurements have been averaged at one minute  
 242 cadence such that the time interval of interest has 441 time points. They have been time  
 243 lagged to the bow shock nose using methods specific to the spacecraft (Farris & Russell,  
 244 1994; Shue et al., 1997). A further time lag is added from the bow shock to the magne-  
 245 topause based on an estimation of the subsolar magnetosheath transit time from (Khan  
 246 & Cowley, 1999).

247 In the HH90 model, the input control variables are IMF  $B_y$ , which is available from  
 248 OMNI, and the transpolar cap voltage  $\Phi_{PC}$ , which is a property of the ionospheric elec-  
 249 tric field (see section 2.4) and hence usually a model output variable. Therefore we need  
 250 an equation to relate  $\Phi_{PC}$  to IMF and solar wind conditions, or other OMNI measure-  
 251 ments. Five such equations are listed below:

#### 252 Lockwood Equation

253 Lockwood and McWilliams (2021) recently used more than 65,000 hourly averages  
 254 of  $\Phi_{PC}$  determined from over 25 years of SuperDARN radar observations to estimate  
 255 the ‘optimum’ solar wind-magnetosphere coupling function.

$$256 \Phi_L = B_{YZ}^{0.64} \rho_{SW}^{0.02} V_{SW}^{0.55} \sin^{2.5}(\theta_{clk}/2) \quad (1)$$

257 where  $B_{YZ}$  is the transverse component of the interplanetary magnetic field, perpendic-  
 ular to the Sun-Earth line.  $\rho_{SW}$  is the mass density,  $V_{SW}$  the solar wind speed, and  $\theta_{clk}$

is the clock angle (Lockwood & McWilliams, 2021). Each of these parameters are available at 1 minute resolution at the bow shock from OMNI, hence  $\Phi_L$  can be calculated at 1 minute cadence, with the lag from the bow shock nose to the magnetosphere added.

## Kp

The equation currently used within TIEGCM and AENeAS (HAO, 2018) is a relationship with Kp. This is a 3-hr index provided as part of the Low Resolution OMNI (LRO) data set by the German Research Centre for Geosciences (GFZ, Potsdam).

$$\Phi_{Kp} = 15 + 15Kp + 0.8Kp^2 \quad (2)$$

An obvious problem with this estimation is that the  $Kp$  index has a cadence of 3 hours and therefore  $\Phi_{Kp}$  does not capture smaller-scale temporal variations. Kp values are supplied every 3 hours, beginning at midnight, and we will use the most up-to-date Kp value at each subsequent time step. Unlike solar wind data which is measured upstream, Kp is not well forecast so is not as useful for a forecasting model. A simplified version of this equation appears in Boyle et al. (1997). According to Boyle et al. (1997) Kp provides a reasonable estimate of  $\Phi_{PC}$  if the IMF has been steady for several hours.

## Polar Cap Index

Ridley and Kihn (2004) show a seasonal trend in the relationship between the Polar Cap Index (PCI) and transpolar voltage, and define a proxy  $\Phi_{PCI}$ :

$$\Phi_{PCI} = 19.28 - 3.31 \sin(T + 1.49) + 17.81PCI, \quad (3)$$

$$T = (\text{month} - 1) \times 2\pi/12 \quad (4)$$

where *month* is the month of the year (i.e. January is *month*=1) and PCI is available as OMNI data. Therefore, this equation is directly comparable to the TS18 and W05 models. It is available at a 1-min cadence but like Kp it is not available in advance, so can not be used for forecasting.

## Boyle Equation

$$\Phi_B = 10^{-4}V^2 + 11.7B \sin^3(\theta_{clk}/2) \quad (5)$$

which is defined such that  $\Phi_B$  is the transpolar voltage in kV,  $V$  is the solar wind bulk velocity in km/s,  $B$  is the IMF magnitude in nT and  $\theta_{clk}$  is the IMF clock angle (Boyle et al., 1997).

## Milan Equation

$$\Phi_D = L_{eff}(V_x)V_x B_{YZ} \sin^{9/2} \frac{1}{2} \theta_{clk}, \quad (6)$$

$$L_{eff}(V_x) = 3.8 \left( \frac{V_x}{4 \times 10^5} \right)^{1/3} \quad (7)$$

where  $\Phi_D$  is the dayside reconnection rate,  $V_x$  is the solar wind speed and  $B_{YZ}$  is the magnitude of the projection of the IMF vector in the  $Y - Z$  GSM plane (Milan et al., 2012).

Some studies have used  $\Phi_{PC}$  as a proxy for dayside reconnection rate (Grocott et al., 2009; P. H. Reiff et al., 1981; P. Reiff et al., 1985). Milan et al. (2012) suggests two flaws in this method. 1) Viscous interaction of the solar wind and the magnetosphere can cause convection without dayside reconnection. 2) The relationship between the two parameters is complex. The intervals used in Milan et al. (2012) had good representation of all clock-angles and values of  $B_{YZ}$  up to 12 nT and solar wind dynamic pressure up to 12 nPa, but few beyond. One issue identified in our results below is very high values of  $\Phi_D$  during storm time intervals.

## 2.4 Model output metrics

To quantitatively compare the models we produce time series of various model metrics that can be extracted from the modelled electric potentials as follows:

### The transpolar voltage

$$\Phi_{PC} = \Phi_{max} - \Phi_{min}, \quad (8)$$

where  $\Phi_{min}$  and  $\Phi_{max}$  are the minimum and maximum electric potentials, respectively. We note that this may not represent the true transpolar voltage if the maximum and minimum potentials are not located at the foci of the dawn and dusk Dungey-cycle convection cells, respectively.

### The polar cap residual

$$\Phi_{res} = \Phi_{max} + \Phi_{min} \quad (9)$$

These two equations provide measures of the strength of the convection and the asymmetry between the dawn and dusk convection cells, respectively.

### Mean polar electric field

The mean electric field magnitude,  $|\bar{EF}|$ , above  $60^\circ$  magnetic latitude, measured in mV/m.

$$|\bar{EF}| = \sum_{\theta, \psi} \frac{|EF|}{N}, \quad (10)$$

where  $\theta \geq 60^\circ$  represents the Altitude Adjusted Corrected GeoMagnetic (AACGM-v2) latitude,  $\psi$  represents all magnetic longitudes, and  $N$  is the number of points. This metric is the mean electric field magnitude above  $60^\circ$  magnetic latitude, measured in mV/m. It allows us to include a measure of the mean strength of the convection for HH90, where  $\Phi_{PC}$  is an input and thus contains limited information about the model performance.

The electric field is calculated using code adapted from part of the Heppner-Maynard-Rich Electric Field Model 1990 (J. P. Heppner, 1977; J. Heppner & Maynard, 1987; Rich & Maynard, 1989). The north-south component of the electric field is calculated at a point,  $\Phi_i$ , by taking the difference of the potential at the point to the north,  $\Phi_{i+1}$ , and the potential at the point to the south,  $\Phi_{i-1}$ , divided by the geographic distance between the two points. The east-west component of the electric field is found in the same way by taking the gradient between a point to the east and west of a point in geographical coordinates.

### Polar cap radius

A proxy for the radius of the polar cap,  $r_{pc}$ , is given by

$$r_{pc} = \frac{1}{2}(\theta_{max} + \theta_{min}) \quad (11)$$

where  $\theta_{max}$  is the colatitude of the location of maximum potential and  $\theta_{min}$  is the colatitude of the location of minimum potential. This measure is a proxy for the radius of the polar cap, with the same caveats as for the transpolar potential.

### Low latitude boundary

A ‘Heppner-Maynard boundary’ (HMB) is routinely determined for all SuperDARN models as the lower-latitude limit of the convection (see table 1). The latitude of this boundary at midnight magnetic local time is specified when performing the spherical harmonic fit. In W05, the low latitude boundary (LLB) is defined by an offset circle (Weimer, 2005). In HH90 there is no LLB. Instead, equatorward of the polar cap boundary, the HH90 electric potential is described by a function that decreases exponentially with decreasing latitude (M. Hairston & Heelis, 1990). For purposes of comparison we will de-

337 fine the HH90 LLB as the latitude across which the mean electric potential drops be-  
 338 low 0.418 kV, which is the mean electric potential of the LLB for W05 throughout the  
 339 time period 7th September 20:00 UT to September 8th 03:20 UT.

### 340 3 Results

#### 341 3.1 Parameterised time series of the September 2017 storm

342 In Figure 2 we present a quantitative comparison of convection pattern parame-  
 343 ters produced by the different models for a time period from 20:00 UT on the 7th to 03:20 UT  
 344 on the 8th September 2017, allowing for a range of IMF conditions during the initial,  
 345 main and recovery phases of the storm. The start and end times of the main phase, as  
 346 found from Sym-H using the method of Walach and Grocott (2019), are shown by the  
 347 vertical, dashed grey lines at 23:07 UT on 7th and 01:08 UT on 8th September. The pa-  
 348 rameters in figure 2 are listed in section 2.4. The vertical, dashed blue lines correspond  
 349 to the snapshots in figure 3.

350 Panel A shows the IMF parameters  $B_y$  and  $B_z$  in blue and orange, respectively.  
 351 The horizontal, dashed line indicates 0 nT. The time interval chosen displays a range of  
 352 IMF conditions, with positive and negative  $B_y$  and  $B_z$  plus a range of IMF clock angles.  
 353 Panel B shows the Sym-H index which is used to define the storm phases (vertical, grey  
 354 lines) as mentioned above. Panel C shows the number of SuperDARN vectors that were  
 355 available at each time point, included to identify to what extent the Map Potential is  
 356 relying on the TS18 model to infill the data gaps. The line-of-sight vectors are combined  
 357 into cells of an equal area polar grid of spatial resolution  $\sim 110 \times 110$  km. The num-  
 358 ber of vectors are then the number of these gridded cells which are occupied by line-of-  
 359 sight vectors. When the number of available vectors is low, Map Potential relies on TS18  
 360 to fill the data gaps. The number of vectors is low throughout the initial phase but in-  
 361 creases to  $\sim 500$  vectors through the peak of the storm.

362 Panel D shows the transpolar voltage proxies from subsection 2.3 equations 1 to  
 363 7. Through the initial phase, whilst IMF  $B_z > \sim -10$  nT, all five proxies perform sim-  
 364 ilarly with values between 100 and 180 kV. When  $B_z$  drops further the IMF and solar  
 365 wind based proxies,  $\Phi_B$  and  $\Phi_D$  (equations 5 and 7), reach huge values of 416 kV and  
 366 631 kV respectively.  $\Phi_L$  (equation 1) has a more conservative but still high value of 337 kV.  
 367 The PCI proxy,  $\Phi_{PCI}$  (equation 4) reaches 306 kV, while the Kp proxy,  $\Phi_{Kp}$  (equation  
 368 2) only reaches 186 kV; Kp is a three-hourly index and so lacks the higher-resolution de-  
 369 tail that is observed in the other three proxies that use 1-minute IMF data. In the fol-  
 370 lowing panels E-H we use the proxies  $\Phi_L$  (equation 3) and  $\Phi_{Kp}$  (equation 2) as the  $\Phi_{PC}$   
 371 input for HH90.

372 Panel E shows the transpolar voltage,  $\Phi_{PC}$ , the difference between the maximum  
 373 and minimum electric potentialx (equation 8) for TiVIE, TS18, W05 and Map Poten-  
 374 tial, as well as the  $\Phi_L$  and  $\Phi_{Kp}$  proxies used in HH90. Considering first the spacecraft-  
 375 based models, HH90 ( $\Phi_L$ ) follows a similar trend to W05 throughout the storm but reaches  
 376 a higher peak of 337 kV at 23:38 UT on the 7th compared to 256 kV for W05. HH90 ( $\Phi_{Kp}$ )  
 377 remains relatively steady at 180-190 kV throughout the main phase and for 2 hours be-  
 378 fore and after it, due to its low 3-hour resolution as already noted in reference to panel  
 379 D. For the SuperDARN-based models  $\Phi_{PC}$  is significantly lower. The TiVIE values are  
 380 elevated throughout the main phase, maximising at 141 kV. TS18 saturates at  $\sim 90$  kV  
 381 when  $B_z = -7$  nT from  $\sim 20:50$  UT and does not change significantly when IMF  $B_z$  con-  
 382 tinues to decrease. This is because the model is at its maximum  $E_{sw}$  bin where the model  
 383 electric potential is averaged over all  $E_{sw} > 3$  mV/m. The Map Potential variation lies  
 384 between TiVIE and TS18. It shows more variation than TS18 and reaches a higher max-  
 385 imum of 124 kV. Map potential tends towards the TS18 model when the number of vec-  
 386 tors is low as the model increasingly relies on the TS18 background model to infill data

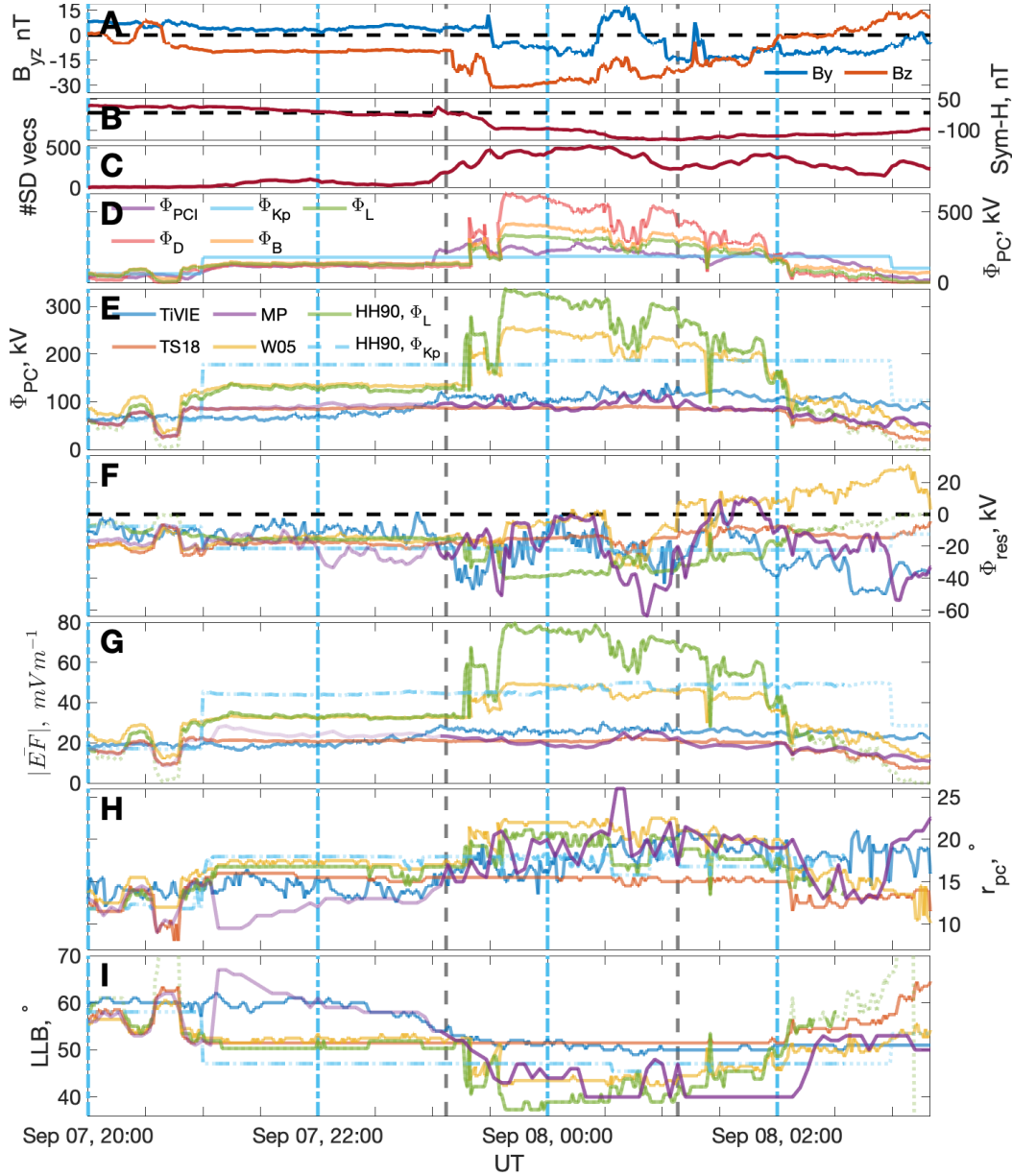


**Figure 2.** Panel A shows  $B_y$  (blue) and  $B_z$  (orange), panel B shows Sym-H, panel C the number of SuperDARN vectors available for the Map Potential, panel D shows five proxies for transpolar voltage,  $\Phi_{PC}$  which are given as equations 2-7. Panel E plots the model outputs for  $\Phi_{PC}$  from TiVIE, TS18, W05 and Map Potential. The models are each represented by the same set of colours in Panels D-I Where Map Potential is calculated from  $< 100$  vectors it is plotted in lighter purple. Panel F shows  $\Phi_{res}$  for the models as in equation 9. Panel G shows the mean electric field above  $60^\circ$  as calculated using equation 10. Panel H and I shows a proxy for the size of the polar cap and lower latitude boundary (LLB) per model, respectively as calculated in section 2.4. Vertical dashed grey lines represent the start and end of the main phase. Vertical dashed blue lines match the snapshots from figure 3.

387  
388

gaps. When there are few SuperDARN vector measurements available ( $< 100$ ), the Map Potential parameter is shown in a lighter shade of purple.

389 Panel F is the residual of the potential, the sum of the maximum and minimum  
 390 potential (equation 9), which we use as a measure of asymmetry between the dawn and  
 391 dusk cells. If  $\Phi_{res} < 0$ , the dusk cell has a stronger magnitude whilst if  $\Phi_{res} > 0$  the  
 392 dawn cell is stronger. Through the main phase of the storm the dusk cell ( $\Phi_{min}$ ) is stronger  
 393 than the dawn cell ( $\Phi_{max}$ ) for all models. Map Potential shows the highest asymmetry  
 394 of any model towards the end of the main phase with  $\Phi_{res} = -64$  kV at 00:52 UT on  
 395 the 8th. During the recovery phase the W05 model has  $\Phi_{res} > 0$ , meaning the dawn  
 396 cell has a higher magnitude. This can be seen in figure 3 at 02:00 UT where  $\Phi_{min} = -73.1$  kV  
 397 and  $\Phi_{max} = 81.7$  kV.

398 Panel G shows the mean electric field vector magnitude  $|\bar{EF}|$  of all vectors above  
 399  $60^\circ$  magnetic latitude (equation 10). The method for calculating electric fields from elec-  
 400 tric potential data is described in section 2.4. Trends in the time series are largely sim-  
 401 ilar to those seen in panel E for  $\Phi_{PC}$  but calculating a parameter from a range of lat-  
 402 itudes and longitudes allows us to include the HH90 response in the comparison. HH90  
 403 ( $\Phi_L$ ) has a similar  $|\bar{EF}|$  to W05 until 23:15 UT on the 7th September, with both hav-  
 404 ing  $|\bar{EF}| \sim 35$  mV/m. From 23:15 UT the HH90 ( $\Phi_L$ ) parameter increases sharply to  
 405 maximise with  $|\bar{EF}| \sim 80$  mV/m, approximately 160% of the maximum value of the  
 406 W05 model. HH90 ( $\Phi_{Kp}$ ) has  $|\bar{EF}| \sim 50$  mV/m from shortly after 21:00 UT on the 7th  
 407 until after 03:00 UT on the 8th. This is higher than the rest of the models until 23:15 UT  
 408 when the  $|\bar{EF}|$  of HH90 ( $\Phi_L$ ) exceeds it and W05 increases to have a similar value un-  
 409 til 02:00 UT. The values from the SuperDARN-based models are again a lot smaller with  
 410 maximum values of  $|\bar{EF}|$  between  $\sim 23$  and  $\sim 31$  mV/m. Again TS18 saturates at  $\sim 20:50$  UT  
 411 whilst TiVIE and Map Potential gradually increase through the main phase.

412 Panel H is a simple proxy for the convection reversal boundary co-latitude which  
 413 is approximated by assuming the location of the maximum and minimum potentials lie  
 414 on a circle containing the polar cap (equation 11). Again the TS18 model saturates at  
 415 moderate IMF conditions with a convection reversal boundary co-latitude of  $\sim 16^\circ$ . HH90  
 416 and W05 show expansion on similar scales to TiVIE and Map Potential throughout the  
 417 main phase, despite having a much larger  $\Phi_{PC}$ . HH90 briefly contracts between 00:35-  
 418 00:51 UT following the increase of  $B_z$  from  $\sim -28$  nT to  $\sim -15$  nT. The Map Pot-  
 419 ential convection map has a smaller radius than the other models during the initial phase  
 420 of the storm of  $9.5^\circ$ , before expanding to have the maximum radius of  $26^\circ$  at 00:40, 8th.  
 421 The other models have average convection reversal boundary co-latitudes located between  
 422  $18^\circ$  and  $22^\circ$ .

423 In panel I we show the LLB for the SuperDARN-based models and W05 which we  
 424 have chosen to be at the midnight boundary. An estimation of the HH90 LLB is included  
 425 as described in section 2.4. Here the models behave very differently. From 20:00-23:00 UT  
 426 on the 7th, the W05, TS18 and HH90 ( $\Phi_L$ ) have a similar LLB, stabilising at  $\sim 50^\circ$ .  
 427 Shortly after 23:00 UT IMF  $B_z$  drops further causing W05, HH90 ( $\Phi_L$ ) and Map Pot-  
 428 ential to lower their boundaries to  $\sim 40^\circ$ . TiVIE has a HMB of  $\sim 60^\circ$  during the initial  
 429 phase which drops down to  $50^\circ$  during the main phase and does not increase significantly  
 430 during the first 130 minutes of the recovery phase. The TS18 HMB remains constant at  
 431  $51.5^\circ$  from 20:50 UT on the 7th to 02:00 UT on the 8th. Map potential and TiVIE, the  
 432 two models that are not defined using IMF and solar wind parameters (unless there are  
 433 few SuperDARN vectors available for Map Potential), extend to lower latitudes much  
 434 later than the other models. Both extend to  $\sim 50^\circ$  latitude for the start of the main phase  
 435 whereas the TS18, HH90 and W05 models extend to  $\sim 50^\circ$  latitude at  $\sim 21:00$  UT.

### 436 3.2 Model comparison of snapshots of convection pattern

437 Figure 3 shows four snapshots of the convection from each of the models, from left  
 438 to right: W05, HH90 ( $\Phi_L$ ) (taking  $\Phi_L$  as the  $\Phi_{PC}$  input), HH90 ( $\Phi_{Kp}$ ), TS18, Map Po-  
 439 tential and TiVIE. From top to bottom the snapshots span 20:00 UT on 7th September

440 to 02:00 UT on 8th September, in two hour intervals. The snapshot times line up with  
 441 vertical blue lines from the time series shown in figure 2 and are chosen to show a range  
 442 of conditions through the initial, main and recovery phases of the storm. The individ-  
 443 ual plots show northern hemisphere convection maps in AACGM-v2 coordinates with  
 444 contour lines drawn at 10 kV intervals. Purple/pink represents negative electric poten-  
 445 tial and blue represents positive electric potential, as shown in the colour bar. A selec-  
 446 tion of metadata including the time, IMF conditions ( $B_Y$  and  $B_Z$ ), SW velocity,  $V$ , Kp,  
 447 Sym-H and the number of SuperDARN vectors ( $\#SD$  vecs) are presented above each row.

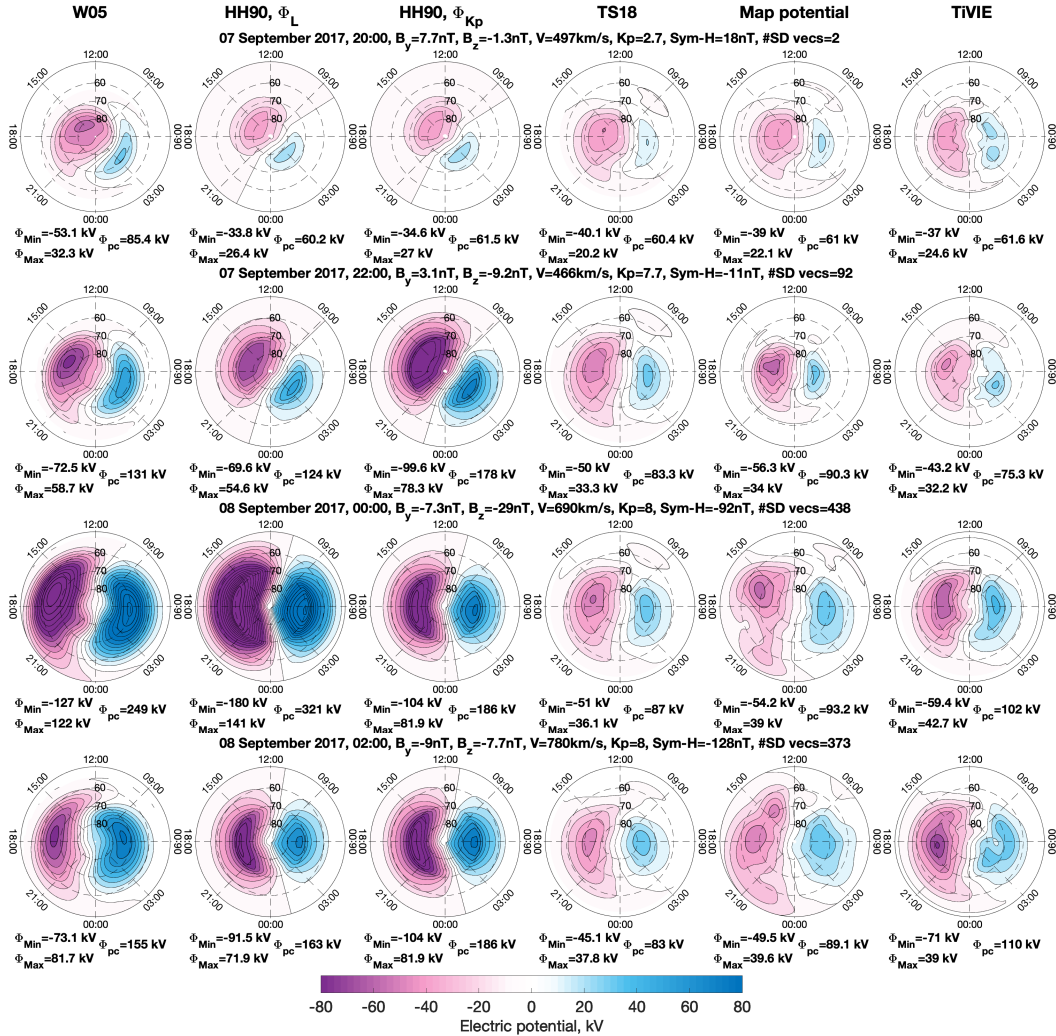


**Figure 3.** Convection maps in magnetic coordinates with contour lines representing 10kV intervals for the models over four time intervals. Purple/pink represents negative electric potential and blue represents positive electric potential, as shown in the colour bar. A selection of parameters including the time, IMF conditions, SW velocity, Kp, Sym-H and the number of SuperDARN vectors are provided per panel. Text below each map shows the maximum and minimum potential on the left and  $\Phi_{PC}$  on the right

448 The first snapshot is during the initial phase when  $B_y = 7.7$  nT and  $B_z = -1.3$  nT.  
 449 The convection map produced by W05 descends to  $\sim 58^\circ$  latitude in the nightside (around

450 midnight) and has a maximum and minimum electric potential at 3 and 15 hours MLT  
 451 respectively. The dusk cell (pink) is centered around  $80^\circ$  latitude, enveloping the mag-  
 452 netic pole, whilst the dawn cell is lower in latitude centered around  $70^\circ$ . The two ver-  
 453 sions of HH90 give similar patterns with low magnitude electric potential with the con-  
 454 vection patterns confined to above  $\sim 67^\circ$  latitude on the nightside. Due to the relatively  
 455 high positive  $B_y$  the zero potential lines are rotated 2 hours clockwise of the midnight  
 456 line and 4 hours clockwise of the noon line. The TS18 convection pattern has a similar  
 457 shape to W05 but TS18 has  $\sim 70\%$  the magnitude of  $\Phi_{PC}$  from W05. The convection  
 458 pattern appears to be rotated  $\sim 3$  hours anti-clockwise compared to W05. The Map Po-  
 459 tential model in this instance has only 2 SuperDARN vectors available and so is almost  
 460 exclusively determined by the TS18 model. TiVIE, parameterised only by storm phase,  
 461 shows a convection pattern for late in the initial phase. The convection pattern resem-  
 462 bles TS18/Map Potential patterns with cells roughly symmetrical about the dawn-dusk  
 463 meridian.

464 By 22:00 UT the W05 pattern has expanded to lower latitudes, rotated anti-clockwise  
 465 and  $\Phi_{PC}$  has increased to 131 kV. HH90 ( $\Phi_L$ ) has maximum and minimum potentials  
 466 with similar locations and magnitudes to W05, but the location of the dayside and night-  
 467 side ‘throats’ is different; note that HH90 defines the zero potential line at  $\sim 9$  and  $\sim$   
 468 23 hours MLT owing to the way the model is parameterised. The locations of these zero  
 469 potential lines are dependent on  $B_y$  and do not allow the positive and negative cells to  
 470 occupy the same local time, in contrast to W05 in the midnight local time sector. HH90  
 471 ( $\Phi_{Kp}$ ) has a higher magnitude  $\Phi_{PC}$  and as such the convection expands equatorward  
 472 by a further  $\sim 2^\circ$  compared to that with the  $\Phi_L$  input. TS18 is a similar shape to W05  
 473 but with much lower  $\Phi_{PC}$  of 83.3 kV. Compared to HH90 it is rotated anti-clockwise by  
 474 several hours, and the nightside throat is rotated anti-clockwise by  $\sim 1$ -2 hours compared  
 475 to W05. Map Potential now has 92 vectors contributing to the fit and so shows a dif-  
 476 ferent picture to TS18 and is constrained to higher latitudes. TiVIE resembles TS18 with  
 477 less uniformity and less asymmetry between the dawn and dusk cells.

478 By 00:00 UT  $B_z$  has reached  $-29$  nT with a SW velocity of 690 km/s, which results  
 479 in very high electric potential magnitudes. W05 has expanded such that the lower lat-  
 480 itude boundary is now located below  $50^\circ$  latitude. The polar cap boundary as inferred  
 481 from the latitude of the cell foci has expanded in comparison to the map at 20:00 UT.  
 482 HH90 ( $\Phi_L$ ) has an even higher  $\Phi_{PC}$  and greater asymmetry between the maximum and  
 483 minimum potentials. Negative IMF  $B_y$  results in an anti-clockwise rotation of  $\sim 2$  hours  
 484 of MLT compared to the previous time interval. HH90 ( $\Phi_{Kp}$ ) has the same input  $\Phi_{PC}$   
 485 as at the previous time point, resulting in a similar convection pattern with any differ-  
 486 ences attributed to the rotation of the convection pattern by 2 hours of MLT due to the  
 487 decrease of  $B_y$ . TS18 has not changed significantly from 22:00 UT because the model has  
 488 reached its maximum  $E_{sw}$  bin. Map Potential extends to lower latitudes and has slightly  
 489 higher potentials than TS18 but much lower potentials than the W05 and HH90 patterns.  
 490 TiVIE is now in the main phase of the storm and reaches a higher  $\Phi_{PC}$  than the other  
 491 SuperDARN models but still much lower than the W05 and HH90 models.

492 The main phase of the storm ends at 01:08 UT, and so the final snapshot at 02:00 UT  
 493 is during the recovery phase of the storm. W05 relies on delayed values of IMF and SW  
 494 conditions and therefore shows a contracted polar cap with a much lower  $\Phi_{PC}$  than the  
 495 previous snapshot. W05 at 02:00 UT is the only map from our chosen snapshots that has  
 496 a higher magnitude dawn cell than dusk cell as  $|\Phi_{max}|$  is higher than  $|\Phi_{min}|$ . HH90 ( $\Phi_L$ )  
 497 likewise uses IMF and SW values so has contracted to higher latitudes. HH90 ( $\Phi_{Kp}$ ) has  
 498 increased very slightly in magnitude due to Kp increasing from 7.7 to 8. Otherwise the  
 499 pattern remains the same as above with a further anti-clockwise rotation due to a fur-  
 500 ther decrease in  $B_y$ . TS18 is still much the same, as the climatology still corresponds  
 501 to its highest  $E_{sw}$  bin. Map Potential, using SuperDARN measurements from the inter-  
 502 val, shows the convection map still extends to lower latitudes (below  $50^\circ$  latitude) and

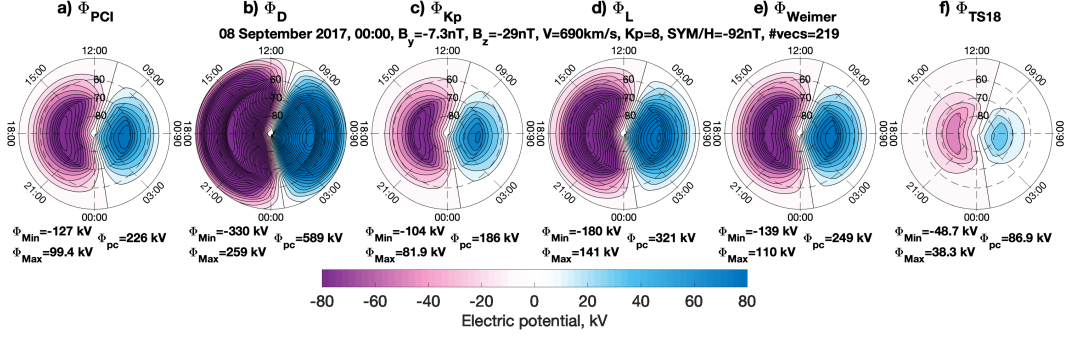


**Figure 4.** Convection maps in magnetic coordinates with contour lines representing 10 kV intervals for the Heelis model with six  $\Phi_{PC}$  proxies are four time intervals. Purple/pink represents negative electric potential and blue positive, as shown in the colour bar. A selection of parameters including the time, IMF conditions, SW velocity, PCI, Sym/H and the number of SuperDARN vectors are provided per panel.

503 still has a similar  $\Phi_{PC}$  ( $\Phi_{PC} \sim 89.1$  kV) than the value during the main phase of the  
 504 storm. TiVIE is now in the recovery phase and mainly shows an increased magnitude  
 505 of the dusk cell from  $-59.4$  kV to  $-71$  kV.

506 Figure 4 highlights how big an effect the choice of the  $\Phi_{PC}$  proxy has on the con-  
 507 vention map output by HH90. We show six examples, all for the same time point of 00:00,  
 508 8th September. From a) to f) we take the input of  $\Phi_{PC}$  to be  $\Phi_{PCI}$  (equation 4),  $\Phi_D$   
 509 (equation 7),  $\Phi_{Kp}$  (equation 2),  $\Phi_L$  (equation 1), followed by the  $\Phi_{PC}$  output by the W05  
 510 and TS18 models at the same time point. The rotation of the pattern remains the same  
 511 for each as it is a function of  $B_y$  which remains the same. However the magnitude of the  
 512 electric potential and the extent to which the pattern expands is very different. Panel  
 513 f) takes the input of  $\Phi_{PC}$  to be that which is output from the TS18 model. As TS18 had  
 514 saturated by this time point,  $\Phi_{pc} = 86.9$  kV is much lower than the other estimates of  
 515  $\Phi_{PC}$  and results in the pattern being confined to above  $\sim 62^\circ$  latitude. At the other  
 516 end of the extremes is panel b) which takes the dayside reconnection rate,  $\Phi_D$  as input.  
 517 This results in  $\Phi_{pc} = 589$  kV,  $6.8\times$  higher than the corresponding value from panel f).  
 518 The remaining maps range from  $\Phi_{PC} = 186$  kV using  $\Phi_{Kp}$  (c) and a  $\Phi_{PC} = 321$  kV  
 519 using  $\Phi_L$  (d). The lower boundary of the pattern extends from  $\sim 58^\circ$  to  $\sim 50^\circ$  with  
 520 the increase in magnitude from c) to d). As it is the Kp equation in c) that is currently  
 521 used within AENeAS we will continue to compare  $\Phi_{Kp}$  input throughout our analysis.  
 522 We will additionally use  $\Phi_L$  as input to HH90 as a comparison because it is the optimum  
 523 coupling-function according to Lockwood and McWilliams (2021), and it has a less ex-  
 524 treme response to the low  $B_z$  values seen within the September 2017 storm.

### 525 3.3 Electric Field Vectors for MLT bands

526 In this section we look in more detail at the variation of the north-south electric  
 527 field component throughout the storm by taking latitudinal slices across the dawn-dusk  
 528 line (6 to 18 MLT) and the noon-midnight line (12 to 24 MLT). The electric field vec-  
 529 tors were calculated from the gradient of the potential using the method specified in sec-  
 530 tion 2.4. We have converted the north-south electric field vector into Cartesian coordi-  
 531 nates such that, along the dawn-dusk line, positive electric field is dawn-to-dusk directed  
 532 (as shown in the left column of figure 5) and along the midnight-noon line positive elec-  
 533 tric field is midnight-to-noon directed (as shown in the right column of figure 5). By look-  
 534 ing at the MLT bands at dawn (MLT=6) to dusk (MLT=18), and noon (MLT=12) to

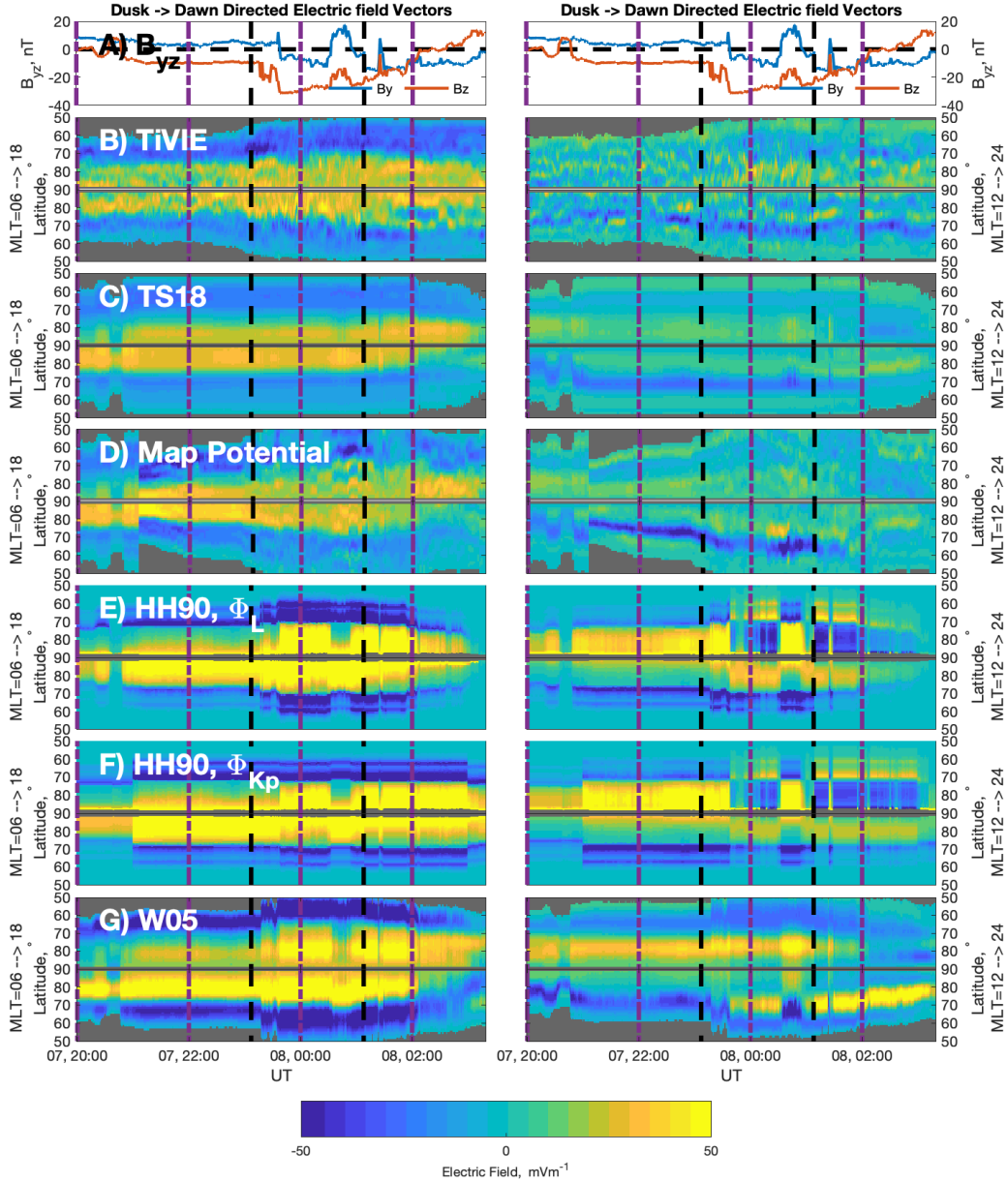


**Figure 5.** Electric field vectors with left column along the dawn-dusk line with dawn-to-dusk direction and the right column is along the midnight-noon line with midnight-to-noon direction. Panel A has IMF  $B_y$  and  $B_z$  for reference. Vertical dashed black lines represent the start and end of the main phase. Vertical dashed purple lines match the snapshots from figure 3.

535 midnight (MLT=24), we see how the topology of the polar cap and lower latitude elec-  
 536 tric field patterns change throughout the storm, as well as the differences in electric field  
 537 magnitude between the different models.

538 In panel A we have plotted the IMF  $B_y$  and  $B_z$  components of the field for easy  
 539 comparison with the EF colour plots. The left column plots the dawn-to-dusk directed  
 540 component of the electric field (EF) according to the colour bar. The x-axis shows the  
 541 time and the y-axis plots latitude where it increases from 50 – 90° latitude along the

542 MLT=6 line, where it crosses the pole and decreases from 90–50° along the MLT=18  
 543 line. The right column plots the midnight-to-noon directed component of the EF along  
 544 the MLT=12 to MLT=24 line. The models are each plotted as rows with B) TiVIE, C)  
 545 TS18, D) Map Potential, E) HH90 ( $\Phi_L$ ), F) HH90 ( $\Phi_{Kp}$ ) and G) W05 from top to bot-  
 546 tom. Colours represent the electric field strength and direction as shown by the colour  
 547 bar. Grey shows where there is no data, either because it is below the LLB, or it is close  
 548 to the magnetic pole.

549 Beginning with the left hand column, we see a dawn-to-dusk directed electric field  
 550 (positive) within the polar cap (corresponding to anti-sunward flow) and a dusk-to-dawn  
 551 directed electric field (negative) at auroral latitudes (corresponding to sunward flow).  
 552 This pattern is consistent across the entire storm with equatorward expansion of the po-  
 553 lar cap and the lower latitude boundary evident throughout the storm. Panels E-G, i.e.  
 554 HH90 ( $\Phi_L$ ), HH90 ( $\Phi_{Kp}$ ), and W05, have higher EF vector magnitudes than the SuperDARN-  
 555 based models in panels B-D, throughout the storm. TiVIE (Panel B) shows significant  
 556 variation, particularly in its dawn-to-dusk directed electric field within the polar cap and  
 557 shows more fine structure compared to the other models. TS18 (Panel C) saturates at  
 558  $\sim 20:50$  UT, as previously seen, and shows a similar pattern from then until 02:00 UT.  
 559 Map potential (Panel D) shows a sharp change at  $\sim 21:06$  UT when the model switches  
 560 from relying heavily on the TS18 climatologies to using available SuperDARN data. Map  
 561 Potential initially has a relatively strong EF magnitude, both within the pole and at au-  
 562 roral latitudes, but this weakens during the main phase of the storm as the pattern ex-  
 563 tends to lower latitudes. At auroral latitudes HH90, with both  $\Phi_L$  and  $\Phi_{Kp}$  (Panels E-  
 564 F) has a two-band structure for the dusk-to-dawn directed vectors, with one band cen-  
 565 tred at around  $\sim 70^\circ$  and a thinner band at  $\sim 60^\circ$  throughout. HH90 has exponentially  
 566 decreasing potential outside of the polar cap so no LLB (low latitude grey zone) is shown;  
 567 the EF magnitude tends towards zero. For all models the overall pattern is reflected across  
 568 the pole but there are some asymmetries between dusk and dawn. Each of the models  
 569 has stronger dawn-to-dusk directed EF within the polar cap on the dawn side compared  
 570 to the dusk side during the initial phase. For TiVIE, TS18, Map Potential and W05 (Pan-  
 571 els B-D and G) this pattern continues throughout the main phase of the storm but the  
 572 HH90 models (Panels E-F) flip to having stronger dusk side EF magnitude within the  
 573 polar cap when IMF  $B_y$  is sufficiently negative e.g. at  $\sim 23:38-00:32$  UT and  $\sim 00:56-$   
 574  $03:18$  UT corresponding to when the IMF  $B_y$  component switches from positive to neg-  
 575 ative. W05 shows enhancements in the dusk-side dawn-to-dusk directed field at the same  
 576 times. TiVIE (Panel B) shows an enhancing dusk-to-dawn directed region of EF (dark  
 577 blue) shortly after the 22:00 UT in the dusk-side auroral zone.

578 The right hand column is along the MLT=12 to 24 line, we generally see a midnight-  
 579 to-noon directed electric field (positive) within the polar cap and a noon-to-midnight di-  
 580 rected electric field (negative) at auroral latitudes but the patterns are less consistent  
 581 than they were along the dawn-dusk line. TiVIE (Panel B) shows more variability with  
 582 instances of positive and negative vectors scattered around a consistent noon-to-midnight  
 583 directed strip (blue) of electric field between 65-75° latitude at noon. TS18 (Panel C)  
 584 shows weak electric field magnitude, particularly below 65°, with the strongest EF be-  
 585 ing noon-to-midnight directed at auroral latitudes on the noon-side. Likewise Map Po-  
 586 tential (Panel D) has relatively weak EF vector magnitude with the strongest vectors  
 587 being noon-to-midnight directed on the noon-side from  $\sim 21:00$  UT, which then expands  
 588 from  $\sim 80$  degree latitude to  $\sim 60^\circ$  by  $\sim 00:30$  UT on the 8th. The noon-side HH90  
 589 models, with both  $\Phi_L$  and  $\Phi_{Kp}$  (Panels E-F) show a weaker but similar pattern to MLT=18.  
 590 However at midnight HH90 very clearly shows where the zero potential line is switch-  
 591 ing from pre to post midnight due to changes in IMF  $B_y$ . If  $B_y = 0$  the zero poten-  
 592 tial line is located at 23.5 hours MLT, with negative  $B_y$  rotating it clockwise, and posi-  
 593 tive  $B_y$  rotating it anti-clockwise, by 0.15 hours per nT. When  $B_y = 0.3$  nT the di-  
 594 rection of the electric field bands switch. A plot showing this can be seen in SI, figure  
 595 S5. W05 (Panel G) has a midnight-to-noon directed EF near the polar cap on the night-

596 side but only very weak EF within the pole on the dayside throughout, except for dur-  
 597 ing the period of positive  $B_y$  around  $\sim 00:30$  UT when it strengthens. When IMF  $B_z$   
 598 drops to less than  $-30$  nT at  $\sim 23:30$  UT there is a strong midnight-to-noon directed EF  
 599 around  $70^\circ$  latitude at noon, forming a clockwise spiral of equatorward-directed EF from  
 600 the high latitude negative EF at  $MLT=18$ , through noon at  $70^\circ$ , through  $MLT=6$  around  
 601  $60^\circ$  and to midnight. This spiral is briefly interrupted at  $MLT = 12$  around  $\sim 00:30$  UT  
 602 by the switch to positive  $B_y$  but reappears around  $01:00$  UT when  $B_y$  returns to neg-  
 603 ative. See figures S2-3, SI for an example of the global EF for snapshots at the times of  
 604 the vertical dashed purple lines.

### 3.4 Direct comparison of models

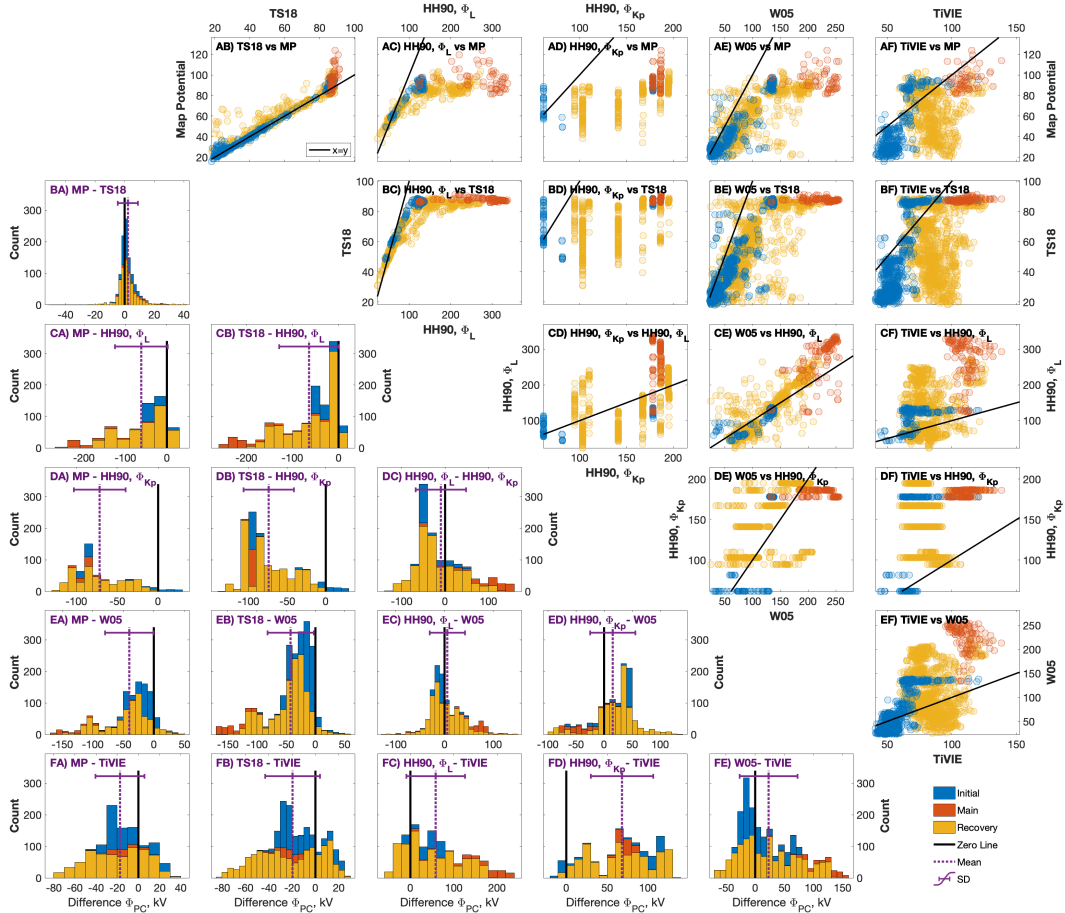


**Figure 6.** Right side: scatter plots of  $\Phi_{PC}$ , kV from model A against that of model B at time  $t$ .  $x=y$  line is in black. Left side: Histogram of  $\Phi_{PC}$ , kV from model A minus that of model B at time  $t$ . The colours represent the phase of the storm at time  $t$ . The histograms are stacked such that the top (blue) represents the initial phase, the middle (orange) the main phase and the bottom (yellow) the recovery phase. The zero difference line is in black, the mean in dashed purple with the standard deviation represented by a horizontal error bar.

606 In Figures 6 and 7 we show a direct comparison of parameters from 11:02 UT, 7th  
 607 September until 23:59 UT, 8th September. This is a much wider time range than con-  
 608 sidered up until now that encompasses all of the initial and main phases of the storm  
 609 and the first third of the recovery phase (23 of 66 hours). For figure 6 the upper half of

610 the matrix has scatter plots plotting the transpolar voltage,  $\Phi_{PC}$ , from model A against  
 611 that of model B at time  $t$ . The  $x = y$  line is included to show where the points would  
 612 lay if the model output was the same. If the points are above the  $x = y$  line the model  
 613 on the  $y$ -axis has a larger  $\Phi_{PC}$  than the model on the  $x$ -axis at that time. For figures  
 614 6 and 7 the times included are from 11:02 UT, 7th September, the start of the initial phase,  
 615 until 23:59 UT, 8th September, during the recovery phase.

616 On the bottom half of the matrix we show histograms of  $\Phi_{PC}$  from model A mi-  
 617 nus  $\Phi_{PC}$  from model B. The black line marks zero difference and is equivalent to  $x=y$ ,  
 618 i.e., if the two models were the same the distribution would be a delta function at zero.  
 619 The mean difference in the models  $\Phi_{PC}$  is overplotted with a dashed purple line with  
 620 the standard deviation represented as a horizontal error bar about the mean.

621 The panels are organised as a grid such that the first row is map potential on the  
 622  $y$ -axis vs each of the models on the  $x$ -axis in each column. The first column shows the  
 623 histograms of map potential minus each of the models. Each row is labelled by the first  
 624 model (A-F) and each column is labelled by the second model (A-F) such that AB) is  
 625 the scatter plot of TS18 vs Map Potential (MP) and the corresponding histogram BA)  
 626 is Map Potential minus TS18. The colours represent the phase of the storm. The his-  
 627 tograms are stacked vertically such that the top (blue) represents the initial phase,  
 628 the middle (orange) the main phase and the bottom (yellow) the recovery phase. The  
 629 histograms are not overlapping i.e. the main phase has the lowest counts as it contains  
 630 the fewest time points.

631 Panel AB) shows that there is a clear saturation in TS18 at  $\sim 90$  kV, with the main  
 632 phase of the storm varying from  $\sim 80$ – $120$  kV for Map potential but  $\Phi_{PC}$  from TS18  
 633 only from  $\sim 85$ – $91$  kV. BA) shows TS18 and Map potential are the most similar, with  
 634 the histogram centred around zero with a slight bias towards Map potential having stronger  
 635  $\Phi_{PC}$  than TS18 (mean difference of 2.3 kV). AC)-AE) show that Map potential saturates  
 636 compared to HH90 and W05. All models but TS18 tend to have stronger  $\Phi_{PC}$  than Map  
 637 Potential for the same time point. This is demonstrated by the points being below the  
 638  $x=y$  line in row A. Similarly, the histograms of Map potential in column A are biased  
 639 towards negative values as all models but TS18 have generally higher  $\Phi_{PC}$ , especially  
 640 during the main phase, and negative mean differences. In the row B scatter plots TS18  
 641 ( $y$ -axis) again shows a clear saturation of  $\sim 90$  kV throughout. In BC) HH90 ( $\Phi_L$ ) is re-  
 642 latively similar to TS18 until this saturation point. In column B each histogram is shifted  
 643 towards negative values and has a negative mean difference showing that  $\Phi_{PC}$  for TS18  
 644 is smaller than each of the other models. In CE) HH90 ( $\Phi_L$ ) and W05 show high cor-  
 645 relation with  $\Phi_L$  generally having slightly higher  $\Phi_{PC}$  than W05. The corresponding his-  
 646 togram EC) is almost centred around zero (mean difference of 5.6 kV) but with a stan-  
 647 dard deviation of 36 kV. During the main phase  $\Phi_L$  can be  $\sim 50$ - $80$  kV higher than that  
 648 of W05.  $\Phi_L$  shows the highest variability compared to the other models with differences  
 649 between  $\Phi_L$  and all models but W05 having a standard deviation of 58 – 68 kV. The  
 650 scatter plots in column/row D show that the  $\Phi_{Kp}$  proxy (equation 2) is ordered in dis-  
 651 crete steps and it consequently does not have much correlation with the other models.  
 652 In column F, TiVIE shows a spread in all cases. Towards the end of the initial phase (in  
 653 blue;  $\sim 20 : 50$  UT to beginning of main phase) TiVIE gradually increases from  $\sim 60$ –  
 654  $120$  kV whilst each of the other models remains constant (as was seen in figure 2).

655 Figure 7 is of the same form as figure 6 but shows a comparison of the LLB/ HMB  
 656 for the models. As for figure 2, the LLB is the HMB for the SuperDARN-based mod-  
 657 els and the LLB at the midnight boundary for W05. An estimation of the HH90 LLB  
 658 is included as described in section 2.4. The convection maps from all but the HH90 mod-  
 659 els are calculated at  $1^\circ$  discrete steps and hence a randomised value between  $\pm 0.5^\circ$  is  
 660 added to the LLB to aid the visualisation of the density of discrete data. Without this  
 661 the discrete points are likely to be overplotted, making it difficult to distinguish between

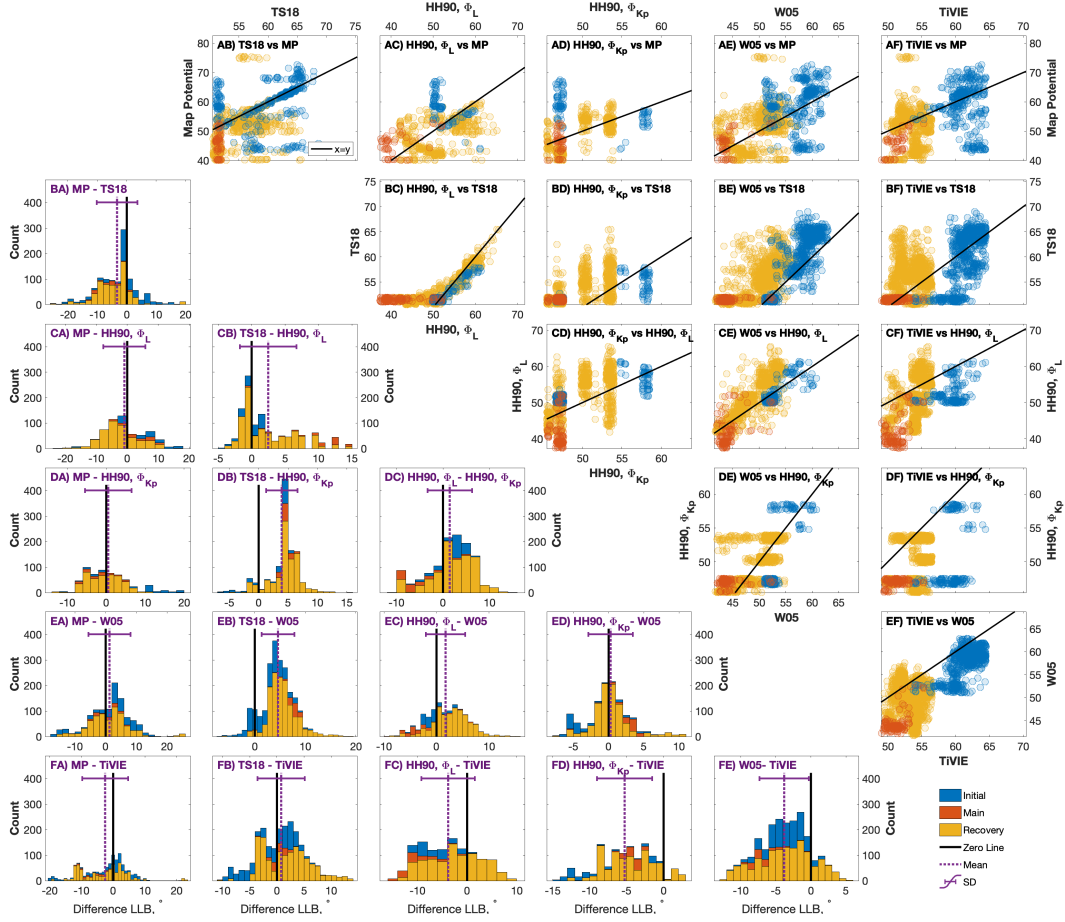


**Figure 7.** Right side: scatter plots of the lower latitude boundary from model A against that of model B at time  $t$ .  $x=y$  line is in black. Left side: Histogram of lower latitude boundary from model A minus that of model B at time  $t$ . The colours represent the phase of the storm at time  $t$ . The histograms are stacked such that the top (blue) represents the initial phase, the middle (orange) the main phase and the bottom (yellow) the recovery phase. The zero difference line is in black, the mean in dashed purple with the standard deviation represented by a horizontal error bar.

662 low and high density data occurrence. The magnetic latitude of HH90 is calculated as  
 663 as described in section S1.2 of the SI.

664 In figure 6 we saw high correlation between  $\Phi_{PC}$  of TS18 and Map Potential. In  
 665 figure 7 we see little correlation between the LLB of TS18 and Map potential in panel  
 666 AB). Map potential generally has a lower boundary than TS18 as indicated by most of  
 667 the points being below the  $x=y$  line, and the negative shifted histogram in BA) which  
 668 has a mean of  $-3.3^\circ$ . Column/row A shows Map potential and the other models have lit-  
 669 tle correlation and a lot of scatter. BC) shows high correlation between HH90 ( $\Phi_L$ ) and  
 670 TS18, until the TS18 LLB saturates at  $51^\circ$  (corresponding to the previous saturation  
 671 seen in electric potential during the main phase of the storm). W05 and TiVIE in columns  
 672 E and F show the LLB at distinct latitude bands in the initial, main and recovery phases.  
 673 For TiVIE (column F) the initial phase has a LLB centred around  $60-65^\circ$ , main  $\sim 50^\circ$   
 674 and recovery  $\sim 52-57^\circ$ . For Weimer (column E) the initial phase has a LLB centred  
 675 between  $50-63^\circ$ , main  $\sim 42-45^\circ$  and recovery  $\sim 42-57^\circ$ . During the initial phase

676 the TiVIE LLB changes from 50–60° whilst TS18, HH90 ( $\Phi_L$ ), HH90 ( $\Phi_{Kp}$ ), and W05  
 677 have a constant lower boundary; this is shown by the horizontal line of blue markers in  
 678 column F. The majority of the histograms are centred around the zero line, with much  
 679 less shift toward the positive/negative than was seen in figure 6. Standard deviations range  
 680 between 2.7° in DB) and 7.2° in FA). Exceptions include TS18 compared to HH90 ( $\Phi_{Kp}$ )  
 681 (DB) and to W05 (EB) which are shifted to the positive i.e., they have a significantly  
 682 lower LLB than TS18, as well as HH90 ( $\Phi_{Kp}$ ) compared to TiVIE (FD) which has a mean  
 683 of -5.3°.

## 684 4 Discussion

685 The aim of this study was to compare the output of modern high-latitude ionospheric  
 686 electric field models, based on SuperDARN measurements, to older models based on space-  
 687 craft data. Electric field models represent an important component of thermospheric mod-  
 688 els due to their influence on Joule heating (Bruinsma et al., 2021). It is possible that in-  
 689 corporating the more modern models into large atmosphere models such as AENeAS will  
 690 improve their forecasting ability. We have compared the versions of the Heelis model (HH90)  
 691 (Heelis et al., 1982; M. Hairston & Heelis, 1990; HAO, 2018), and the Weimer model (W05)  
 692 (Weimer, 2005) that are both implemented in AENeAS with the Thomas and Shepherd  
 693 (TS18) (Thomas & Shepherd, 2018) and TiVIE mode 3 models (Walach & Grocott, 2022),  
 694 as well as the SuperDARN Map Potential (Ruohoniemi & Baker, 1998), during the Septem-  
 695 ber 2017 geomagnetic storm. During geomagnetic storms, Joule heating is significantly  
 696 enhanced. Hence, it is important to be able to forecast well for storm time conditions.  
 697 In this section we highlight the differences in the electric field contribution to Joule heat-  
 698 ing that arise from the different models during storm times and the possible reasons for  
 699 the differences.

700 Although we are only studying a single storm it encompasses a wide range of solar  
 701 wind and IMF conditions to highlight differences in both the model topologies and  
 702 magnitudes. The W05, HH90 ( $\Phi_L$ ) and TS18 models are calculated using 1-min cadence  
 703 solar wind and IMF data as input, and as such are directly sensitive to the variability  
 704 in these parameters. HH90 ( $\Phi_{Kp}$ ) is dependent on the 3-hourly Kp index as well as 1-  
 705 minute cadence IMF  $B_y$ . TiVIE is parameterised by storm phase and so is not directly  
 706 sensitive to variations in the solar wind drivers but is designed to better capture the time  
 707 history of the magnetospheric response. As a forecast model, however, TiVIE is limited  
 708 by the need to await the start and end of each storm phase. Map Potential uses Super-  
 709 DARN measurements of the event, so it is not suitable for forecasting either but can act  
 710 as a baseline, with the caveat that two of the other models we are comparing it to are  
 711 also based on SuperDARN data.

712 The variations in the magnitudes of the electric potential outputs across the ob-  
 713 served range of conditions highlight some of the main differences between the models.  
 714 Under quiet and moderate conditions the models display relatively similar outputs. This  
 715 is particularly clear during the initial and recovery phases in figure 6. Hence, we would  
 716 expect estimates of Joule heating to be relatively consistent between models at these times.  
 717 However, when IMF  $B_z$  drops towards -30 nT, the spacecraft-based models (W05 and  
 718 HH90) can have more than double the transpolar voltage of the SuperDARN-based mod-  
 719 els. This would relate to a difference in Joule heating estimates of more than a factor  
 720 of 4.

721 For the TS18 model the primary reason for the underestimation with respect to  
 722 the spacecraft-based models is simple. When  $B_z < -10$  nT in Figure 2,  $\Phi_{PC}$ ,  $r_{pc}$ , and  
 723 HMB in TS18 all saturate at  $\sim 90$  kV,  $15^\circ$ , and  $51^\circ$ , respectively. This is because  $E_{sw} >$   
 724  $3$  mV/m,  $110 < \theta_{clk} < 250^\circ$ , and dipole tilt is neutral during this time. In this range,  
 725 there are only three potential patterns available in the TS18 model which all have quite  
 726 similar  $r_{pc}$  and HMB and  $\Phi_{PC}$  only varies between 84 and 91 kV (see figure 6 and Ta-

727 ble 2 of TS18). The data used in TS18 was collected during solar cycle 24, which was  
 728 a much less active solar cycle than solar cycle 21, when the data used in W05 was col-  
 729 lected (see figure 1). Thomas and Shepherd (2018) lowered their solar wind electric field  
 730 magnitude,  $E_{sw}$  bins to account for the smaller measurements compared to previous Su-  
 731 perDARN models (Ruohoniemi & Greenwald, 1996; Pettigrew et al., 2010; Cousins &  
 732 Shepherd, 2010). This restriction suggests that this model is not wholly suitable for de-  
 733 scribing variations in convection during extreme storm times. This is unsurprising given  
 734 the model is designed as a background model for the Map Potential. Thomas and Shep-  
 735 herd (2018) have a Kp counterpart statistical characterisation of ionospheric convection  
 736 which is parameterised by Kp and IMF clock angle. The highest Kp bin ( $< 8$ ) shows a  
 737  $-B_z$  convection pattern that extends to lower latitudes on the nightside and has higher  
 738 magnitude electric potential than the highest  $E_{sw}$  bin ( $3.0 \leq E_{SW} < 20.0$  mV/m (Thomas  
 739 & Shepherd, 2018). The maximum value of  $\Phi_{PC}$  using the Kp version of TS18 is  $\sim 97$  kV  
 740 which is still below the maximum values of  $\Phi_{PC}$  found using each of the other models  
 741 during this September 2017 event.

742 For Map Potential the  $E_{sw}$  constraint is partly removed because of the addition  
 743 of SuperDARN measurements from the September 2017 storm itself.  $r_{pc}$  and HMB ex-  
 744 pand equatorward to latitudes comparable to W05 and HH90 ( $\Phi_L$ ) but  $\Phi_{PC}$  for Map  
 745 Potential increases to  $< \sim 120$  kV (30% increase) compared to  $> \sim 200$  kV for W05 and  
 746 HH90 ( $\Phi_L$ ). This suggests that either the large-scale  $\Phi_{PC}$  measure is still heavily con-  
 747 strained by the TS18 model and/or other factors are at play. Firstly, SuperDARN has  
 748 been known to underestimate the  $\Phi_{PC}$  when the polar cap expands beyond the field of  
 749 view of the radars (S. Shepherd et al., 2002). Since this study, the SuperDARN network  
 750 has expanded to both higher and lower latitudes. However, Thomas and Shepherd (2018)  
 751 acknowledge that during extreme events  $\Phi_{PC}$  is likely to underestimated due to the con-  
 752 vection pattern expanding equatorwards of the mid-latitude radars. This may be the case  
 753 for the extreme storm time variations considered here as the HMB saturates at  $40^\circ$ , which  
 754 is an artificial limit in the model due to the lowest available latitude of radar measure-  
 755 ment. Secondly, it has also been noted that when compared to DSMP ion drifts, Super-  
 756 DARN velocities have been shown to be smaller (Drayton et al., 2005). Doppler veloc-  
 757 ities measured by SuperDARN are progressively under-estimated with decreasing iono-  
 758 spheric refractive index caused by increasing electron density (Gillies et al., 2009), which  
 759 may be expected due to enhanced auroral particle precipitation during higher  $\Phi_{PC}$  and  
 760 corresponding geomagnetic activity.

761 For TiVIE, although it is not constrained by TS18, it is based on SuperDARN data  
 762 and so could be underestimating  $\Phi_{PC}$  during extreme events due to the refractive in-  
 763 dex and the pattern extending beyond the equatorward extent of the radars; indeed the  
 764 TiVIE HMB saturates close to  $50^\circ$ , like TS18. Alternatively, or additionally, TiVIE mode  
 765 3 is calculated from 54 storms during solar cycle 24, the same time period as TS18, of  
 766 which only two storms (Sep 26, 2011 and June 22, 2015) have a more negative  $B_z$  than  
 767 that seen in the September 7th-8th, 2017 storm. Likewise, only two (Mar 09, 2012 and  
 768 June 22, 2015) have Kp higher than or equal to that seen in the Sep 7, 2017 storm, mean-  
 769 ing this storm is towards the more extreme end of the events used within TiVIE. This  
 770 could suggest that TiVIE is biased to underestimate  $\Phi_{PC}$  during more extreme storms  
 771 than the average storm of solar cycle 24. However, one feature of TiVIE is that it does  
 772 provide a forecast of the temporal variability introduced to the convection electric field  
 773 during a storm by the inclusion of time history. The delayed solar wind values used as  
 774 input for W05, HH90 and TS18 may result in over or under estimations of the magni-  
 775 tude of  $\Phi_{PC}$  as these models take no account of how long the  $B_z$  component has been  
 776 negative, which is an indication of how much energy has been added to the system through  
 777 reconnection.

778 In contrast to the TS18 and TiVIE models whose solutions are binned averages that  
 779 are constrained to the ranges of the data used in their development, there is no such re-

780 striction in the HH90 and W05 models. By construction, the ionospheric electric poten-  
 781 tial solution in these models is described by parameters that are continuous functions  
 782 of the input control variables, allowing the solutions to be extrapolated even beyond the  
 783 range of the underlying observations. However the choice of parameter functions differs  
 784 within the HH90 model and between it and the W05 model. For HH90 the strong po-  
 785 tentials seen during the main phase of the storm are a result of the input parameter  $\Phi_{PC}$ ;  
 786 the maximum potential in the dawn cell is always 44% of  $\Phi_{PC}$  and minimum potential  
 787 in the dusk cell is always  $-56\%$  of  $\Phi_{PC}$ . Maps showing the effect of the choice of  $\Phi_{PC}$   
 788 proxy are included in figure 4, clearly showing how the choice of this input parameter  
 789 affects the size and magnitude of the convection pattern.

790 The  $\Phi_{PC}$  output from the W05 model is most similar to the Lockwood parame-  
 791 ter  $\Phi_L$ , which we used in HH90 but the W05 model does contain a saturation curve that  
 792 levels to a gradual slope at higher magnitudes of the solar wind electric field (Weimer,  
 793 2005) (equation 3 in Weimer (2005)). There have been many observational, theoretical,  
 794 and modelling studies e.g. (M. R. Hairston et al., 2005; S. G. Shepherd, 2007; Kubota  
 795 et al., 2017), that have found saturation of  $\Phi_{PC}$  for large  $E_{SW}$ . S. G. Shepherd (2007)  
 796 suggests  $\Phi_{PC}$  saturates at  $< 300$  kV whilst Lockwood and McWilliams (2021) suggests  
 797 a typical value between 150–200 kV. Figure S7 plots  $E_{SW}$  vs  $\Phi_{PC}$  which shows the sat-  
 798 uration of W05 at  $\sim 250$  kV to be much higher than the artificial saturation of the Su-  
 799 perDARN based models and  $\Phi_{Kp}$ .  $\Phi_L$  shows a curved relationship with  $E_{SW}$  similar to  
 800 W05 for lower values but it does not saturate.

801 The polar cap radius proxy,  $r_{pc}$  and the lower latitude boundary (or HMB) vari-  
 802 ations show both boundaries moving equatorward throughout the main phase of the storm  
 803 as the  $\Phi_{PC}$  increases. The HH90 ( $\Phi_L$ ) and HH90 ( $\Phi_{Kp}$ ) polar caps are smaller than or  
 804 similar in size to many of the other models despite having a considerably higher  $\Phi_{PC}$ .  
 805 The equation HH90 used to define the convection flow reversal circle is  $\theta_0 = -3.8^\circ +$   
 806  $8.48^\circ \Phi_{pc}^{0.1875}$ , similar to equations found in G. L. Siscoe (1982) and M. Hairston and Heelis  
 807 (1990). Although this is not the same as the polar cap radius proxy we have chosen to  
 808 represent the size of the polar cap (equation 11), it provides an estimate of how big the  
 809 defined HH90 radius can be (see figure S6 in SI). No other model is restricted by this  
 810 equation; they can have larger polar cap radii per  $\Phi_{PC}$  than HH90. The expanding-contracting  
 811 polar cap (ECPC) paradigm (G. Siscoe & Huang, 1985; Lockwood & Cowley, 1992; Mi-  
 812 lan et al., 2007) defines the rate of change of open flux in the polar ionosphere as the dif-  
 813 ference between dayside and nightside reconnection rates. Open flux increases when day-  
 814 side reconnection exceeds nightside reconnection and decreases when nightside recon-  
 815 nection exceeds dayside reconnection. While the dayside reconnection rate is directly re-  
 816 lated to interplanetary conditions, the nightside rate is only weakly related to the IMF;  
 817 it is dependent on the magnetic shear across the magnetotail current sheet (Lockwood  
 818 et al., 2009). Therefore whilst it is likely that a large  $\Phi_{PC}$  will be associated with an in-  
 819 creased polar cap size, it cannot be directly attributable. A large  $\Phi_{PC}$  driven equally  
 820 by dayside and nightside reconnection would not impact the size of the polar cap, and  
 821 a large  $\Phi_{PC}$  driven predominantly by nightside reconnection would cause the size of the  
 822 polar cap to shrink.

823 As with the polar cap boundary variation, the LLBs are also highly variable. HH90  
 824 does not have a strict LLB as it is an exponentially decreasing function equatorward of  
 825 the convection reversal boundary. However, we define a potential magnitude that pro-  
 826 vides an estimate of where the boundary would be (equivalent to the W05 mean poten-  
 827 tial at the midnight HMB). Figure 3 and figure 5 show that the HH90 convection does  
 828 not extend to as low a latitude as many of the other models. HH90 does not have  $|EF| >$   
 829  $25$  mV/m in the north-south component below  $60^\circ$  magnetic latitude at dawn or dusk,  
 830 or at midnight or noon at any point during our time interval; all other models extend  
 831 equatorward of this. However in figure 2, HH90 ( $\Phi_L$ ) has a lower boundary similar to  
 832 W05 and Map Potential through the main phase of the storm. Figure 7 shows the bound-

ary from HH90 ( $\Phi_L$ ) to be lower than each of the other models during the main phase. In terms of the HMB, TiVIE has similar limits to TS18, despite its saturation. W05 and Map Potential extend  $\sim 10^\circ$  lower than TiVIE and TS18 during the main phase. Part of this may be due to the issues with poor HMB placement using the current algorithm within Map Potential (Fogg et al., 2020).

The fixed HH90 shape is also worth mentioning. The zero potential lines at midnight and noon are defined solely by the value of IMF  $B_y$ . The convection cells cannot overlap in MLT so this line is critical to the shape and longitudinal spread of the dawn and dusk cells. AENeAS hard codes limits of  $-11 \leq B_y \leq 7$  nT to restrict the placement of the zero potential line in the northern hemisphere to stop the pattern rotating excessively and the potential at the centre of the pattern having a higher potential than the maximum and minimum values seen at the centre of the convection cells. However, this presents further problems with these defined boundaries during times of strong IMF  $B_y$ . It is clear from the snapshots in figure 3 that large changes in  $B_y$  have a significant effect on the rotation of the HH90 convection pattern, a rotation that is not obvious in the other models. In terms of the north-south component of the electric field, small changes in IMF  $B_y$  result in sign changes in the electric field measured at noon and midnight. This effect is highlighted in SI figure S5. Figure 5 further highlights the problems with the fixed boundary at 24:00 MLT. The electric field switches from strongly positive to strongly negative, and vice-versa, due to longitudinal changes in the location of the zero potential line that are purely a function of  $B_y$  variability. If  $B_y = 0$ , the zero potential line enters at 23.5 hours MLT, with negative  $B_y$  rotating it clockwise, and positive  $B_y$  rotating it anti-clockwise, by 0.15 hours per nT. When  $B_y < 0.3$  nT the direction of the electric field bands switch.

The differences in both the size of the polar cap and the latitude of the LLB between the different models are important as they will have knock on effects in atmospheric models like AENeAS. For example, if a model places the LLB at too high a latitude then a region will be predicted to have zero electric field instead of a non-zero electric field and this will impact Joule heating estimates. The effects on Joule heating are less straightforward in terms of the radius of convection reversal (for which we use the polar cap radius proxy,  $r_{pc}$ ) but it is possible to envisage a situation where, if  $r_{pc}$  is changing, the electric field direction is likely to be switching (as the boundary moves above and below a given geographical region). We know from Deng et al. (2009) that electric field variability (and not just magnitude) is key to Joule heating.

## 5 Conclusions

Models of the high-latitude ionospheric electric field are commonly used to specify the magnetospheric forcing in modern atmosphere models. The use of decades-old spacecraft-based models is still widespread. However, modern radar-derived electric field models could improve forecasting functionally. We have compared the AENeAS version of the Heelis model (Heelis et al., 1982; M. Hairston & Heelis, 1990; HAO, 2018) referred to as HH90, the Weimer model (W05) (Weimer, 2005), Thomas and Shepherd (TS18) (Thomas & Shepherd, 2018) and TiVIE (Walach & Grocott, 2022), as well as the SuperDARN Map Potential. Here we compare the electric field models during the September 2017 storm, covering a range of solar wind and IMF conditions. We explore the relationships between the IMF conditions and model output parameters and find:

- TS18 consistently has the lowest electric potential output and does not expand to low latitudes during the September 2017 storm. This is primarily because the TS18 model was developed using data from the relatively benign solar cycle 24 and has only one ionospheric electric potential solution for a solar wind electric field value  $E_{sw} > 3$  mV/m (for given IMF  $B_y$  and dipole tilt). Thus TS18 is not suitable for use in AENeAS during storm times. If this model could be extended

- 884 using a much larger SuperDARN data set over multiple solar cycles then it might  
 885 be possible to produce a more accurate model version.
- 886 • TIVIE mode 3 is parameterised by storm phase timings, not IMF and SW con-  
 887 ditions. Its output therefore misses details associated with the individual storm.  
 888 This variability could be captured by introducing additional parameterisation to  
 889 TiVIE. Like TS18, TiVIE was developed using data from solar cycle 24 and thus  
 890 is biased to ionospheric electric potential solutions appropriate to weaker storms.
  - 891 • HH90 is hugely dependent on the  $\Phi_{PC}$  proxy used as input. HH90 based on Kp  
 892 (as used in AENeAS) has very poor temporal resolution which makes it unsuit-  
 893 able for many applications. To use HH90 requires a potential proxy that has been  
 894 well tested in storm conditions.
  - 895 • HH90 ( $\Phi_L$ ) is comparable to Weimer in electric potential magnitude and convec-  
 896 tion pattern topology but the transpolar voltage differs by  $\sim 50\%$  during peak storm  
 897 times.

898 Based on these findings we conclude that the main difference between models is  
 899 that the parameters of the spacecraft-based electric potential solutions are fit to a con-  
 900 tinuous function of the input control variables, whereas the SuperDARN-based solutions  
 901 are averages for comparable observed input conditions (e.g., binned by  $E_{sw}$ , or time within  
 902 the storm). Consequently, the spacecraft-based models are designed to extrapolate to  
 903 extreme conditions even beyond those observed whereas the SuperDARN-based mod-  
 904 els are constrained to the conditions available within the data used to develop them. This  
 905 causes the SuperDARN-based model metrics to reach an artificial limit for rare extreme  
 906 conditions, such as the apparent saturation of the transpolar voltage at  $\sim 100$  kV. This  
 907 is also exacerbated by the known systematic under-estimation of the ionospheric elec-  
 908 tric field by high frequency radars due to the ionospheric refractive index being less than  
 909 the assumption of unity and limits introduced by the low latitude extent of the Super-  
 910 DARN radars. However, whilst the spacecraft-based models have no such limits, their  
 911 solutions have high uncertainty because they are based on limited data or are extrap-  
 912 olations beyond the observed range based on equations with different functional forms.

913 Consequently, we recommend that efforts to nowcast and forecast the thermosphere  
 914 using ensemble models such as AENeAS include an analysis of the effects of the uncer-  
 915 tainties in the underlying electric field models. This could be achieved by comparing the  
 916 degree of satellite drag predicted using such models to direct satellite drag observations.  
 917 In addition, more work should be done in further developing ionospheric electric field mod-  
 918 els during geomagnetic storms, especially by including more data from periods of high  
 919 geomagnetic activity. A greater understanding of the relevant physics such as transpo-  
 920 lar voltage saturation and the refractive index effect are needed to bring the model pre-  
 921 dictions closer together.

## 922 6 Open Research

923 The version of the Heelis model used for the analysis in this paper is taken from  
 924 TIEGCM (Qian et al., 2014), a model within AENeAS (Elvidge & Angling, 2019; HAO,  
 925 2018). A full description of the code is included in the SI. A full version of TIEGCM code  
 926 can be downloaded from <https://www.hao.ucar.edu/modeling/tgcm/download.php>.  
 927 The W05 code was provided by D. Weimer. It is available as an IDL model (Weimer,  
 928 2019), but the version used in this paper is the Fortran 90 code used within TIEGCM  
 929 and is available as part of the aforementioned download. TS18 is available using the ‘solve\_model’  
 930 module as part of the Radar Software Toolkit (RST Version 4.6) (SuperDARN Data Anal-  
 931 ysis Working Group et al., 2021), available for download at [https://superdarn.github](https://superdarn.github.io/dawg/software/)  
 932 [.io/dawg/software/](https://superdarn.github.io/dawg/software/). Map Potential and TiVIE were processed using the ‘maptoefield’  
 933 RST module to find the electric potential from the fit.map files. The Map Potential data  
 934 processing is described fully in (Walach et al., 2022) and we use the equivalent of their

935 ‘D4’ dataset. This includes data from all the northern hemisphere radars, which were  
 936 processed using a range gate limit from 800-2000km and the TS18 background model.  
 937 Where there are data gaps, model vectors are infilled from the TS18 background model.  
 938 TiVIE storm mode phases are available from the Lancaster University’s research archive  
 939 (PURE), Ionospheric Electric Field Morphologies during Geomagnetic Storm Phases 2.0,  
 940 <https://doi.org/10.17635/lancaster/researchdata/417>. Heppner-Maynard-Rich  
 941 Electric Field Model 1990 available from [https://git.smce.nasa.gov/ccmc-share/  
 942 modelwebarchive/-/tree/main/Heppner-Maynard-Rich\\_Electric-Field-Model](https://git.smce.nasa.gov/ccmc-share/modelwebarchive/-/tree/main/Heppner-Maynard-Rich_Electric-Field-Model). Sunspot  
 943 data is from <https://www.sidc.be/silso/infosmntot> (downloaded 14th October 2021).  
 944 NASA OMNI data is available at <http://omniweb.gsfc.nasa.gov/ow.html> (downloaded  
 945 19th January 2021). Conversion from magnetic coordinates to geographic is calculated  
 946 using the AACGM-v2 library (S. Shepherd, 2014; Burrell et al., 2020). The SuperDARN  
 947 data are available from the BAS SuperDARN data mirror [https://www.bas.ac.uk/project/  
 948 superdarn](https://www.bas.ac.uk/project/superdarn).

## 949 Acknowledgments

950 We would like to thank the SWIMMR consortium members for useful discussions and  
 951 D. Weimer for provision of the W05 model. The authors acknowledge the use of Super-  
 952 DARN data. SuperDARN is a collection of radars funded by the national scientific fund-  
 953 ing agencies of Australia, Canada, China, France, Italy, Japan, Norway, South Africa,  
 954 UK, and United States. The work presented in this paper was supported by Natural En-  
 955 vironment Research Council grants NE/V00283X/1 and NE/V002686/1 (LO, AG), NE/P001556/1  
 956 and NE/T000937/1 (AG, M-TW), and NE/V002732/1 (MML, GC, MPF, RMS).

## 957 References

- 958 Boyle, C., Reiff, P., & Hairston, M. (1997). Empirical polar cap potentials. *Journal*  
 959 *of Geophysical Research: Space Physics*, *102*(A1), 111–125.
- 960 Bristow, W. A., Topliff, C., & Cohen, M. B. (2022). Development of a high-latitude  
 961 convection model by application of machine learning to superdarn observa-  
 962 tions. *Space Weather*, *20*(1), e2021SW002920.
- 963 Bruinsma, S., Boniface, C., Sutton, E. K., & Fedrizzi, M. (2021). Thermosphere  
 964 modeling capabilities assessment: geomagnetic storms. *Journal of Space*  
 965 *Weather and Space Climate*, *11*, 12.
- 966 Burrell, A., van der Meer, C., & Laundal, K. M. (2020, January). *abur-*  
 967 *rell/aacgm2: Version 2.6.0*. Zenodo. Retrieved from [https://doi.org/  
 968 10.5281/zenodo.3598705](https://doi.org/10.5281/zenodo.3598705) doi: 10.5281/zenodo.3598705
- 969 Chisham, G., Lester, M., Milan, S. E., Freeman, M. P., Bristow, W. A., Grocott,  
 970 A., ... Walker, A. D. M. (2007). A decade of the Super Dual Auroral Radar  
 971 Network (SuperDARN): scientific achievements, new techniques and future  
 972 directions. *Surveys in Geophysics*, *28*, 33-109.
- 973 Cousins, E., & Shepherd, S. (2010). A dynamical model of high-latitude convection  
 974 derived from superdarn plasma drift measurements. *Journal of Geophysical Re-*  
 975 *search: Space Physics*, *115*(A12).
- 976 Deng, Y., Maute, A., Richmond, A. D., & Roble, R. G. (2009). Impact of electric  
 977 field variability on joule heating and thermospheric temperature and density.  
 978 *Geophysical Research Letters*, *36*(8).
- 979 Dickinson, R. E., Ridley, E., & Roble, R. (1981). A three-dimensional general cir-  
 980 culation model of the thermosphere. *Journal of Geophysical Research: Space*  
 981 *Physics*, *86*(A3), 1499–1512.
- 982 Dimmock, A. P., Rosenqvist, L., Hall, J.-O., Viljanen, A., Yordanova, E., Honkonen,  
 983 I., ... Sjöberg, E. (2019). The gic and geomagnetic response over fennoscand-  
 984 ia to the 7–8 september 2017 geomagnetic storm. *Space Weather*, *17*(7),  
 985 989–1010.

- 986 Drayton, R., Koustov, A., Hairston, M., & Villain, J.-P. (2005). Comparison of  
 987 dmsp cross-track ion drifts and superdarn line-of-sight velocities. In *Annales*  
 988 *geophysicae* (Vol. 23, pp. 2479–2486).
- 989 Elvidge, S., & Angling, M. J. (2019). Using the local ensemble transform kalman fil-  
 990 ter for upper atmospheric modelling. *Journal of Space Weather and Space Cli-*  
 991 *mate*, 9, A30.
- 992 Farris, M., & Russell, C. (1994). Determining the standoff distance of the bow  
 993 shock: Mach number dependence and use of models. *Journal of Geophysical*  
 994 *Research: Space Physics*, 99(A9), 17681–17689.
- 995 Fogg, A., Lester, M., Yeoman, T., Burrell, A., Imber, S., Milan, S., . . . Anderson,  
 996 B. (2020). An improved estimation of superdarn heppner-maynard boundaries  
 997 using ampere data. *Journal of Geophysical Research: Space Physics*, 125(5),  
 998 e2019JA027218.
- 999 Gillies, R., Hussey, G., Sofko, G., McWilliams, K., Fiori, R., Ponomarenko, P., &  
 1000 St.-Maurice, J.-P. (2009). Improvement of superdarn velocity measurements by  
 1001 estimating the index of refraction in the scattering region using interferometry.  
 1002 *Journal of Geophysical Research: Space Physics*, 114(A7).
- 1003 Grocott, A., Badman, S. V., Cowley, S., Milan, S. E., Nichols, J. D., & Yeoman,  
 1004 T. K. (2009). Magnetosonic mach number dependence of the efficiency of  
 1005 reconnection between planetary and interplanetary magnetic fields. *Journal of*  
 1006 *Geophysical Research: Space Physics*, 114(A7).
- 1007 Hairston, M., & Heelis, R. (1990). Model of the high-latitude ionospheric convection  
 1008 pattern during southward interplanetary magnetic field using de 2 data. *Jour-*  
 1009 *nal of Geophysical Research: Space Physics*, 95(A3), 2333–2343.
- 1010 Hairston, M. R., Drake, K. A., & Skoug, R. (2005). Saturation of the ionospheric  
 1011 polar cap potential during the october–november 2003 superstorms. *Journal of*  
 1012 *Geophysical Research: Space Physics*, 110(A9).
- 1013 HAO. (2018). *Tiegcmm v1.94 model description*. Retrieved from [https://www.hao](https://www.hao.ucar.edu/modeling/tgcm/doc/description/model.description.pdf)  
 1014 [.ucar.edu/modeling/tgcm/doc/description/model.description.pdf](https://www.hao.ucar.edu/modeling/tgcm/doc/description/model.description.pdf)
- 1015 Heelis, R., Lowell, J. K., & Spiro, R. W. (1982). A model of the high-latitude iono-  
 1016 spheric convection pattern. *Journal of Geophysical Research: Space Physics*,  
 1017 87(A8), 6339–6345.
- 1018 Heppner, J., & Maynard, N. (1987). Empirical high-latitude electric field models.  
 1019 *Journal of Geophysical Research: Space Physics*, 92(A5), 4467–4489.
- 1020 Heppner, J. P. (1977). Empirical models of high-latitude electric fields. *Journal of*  
 1021 *Geophysical Research*, 82(7), 1115–1125.
- 1022 Khan, H., & Cowley, S. (1999). Observations of the response time of high-latitude  
 1023 ionospheric convection to variations in the interplanetary magnetic field using  
 1024 eiscat and imp-8 data. In *Annales geophysicae* (Vol. 17, pp. 1306–1335).
- 1025 Kubota, Y., Nagatsuma, T., Den, M., Tanaka, T., & Fujita, S. (2017). Polar cap  
 1026 potential saturation during the bastille day storm event using global mhd sim-  
 1027 ulation. *Journal of Geophysical Research: Space Physics*, 122(4), 4398–4409.
- 1028 Liu, H.-L., Bardeen, C. G., Foster, B. T., Lauritzen, P., Liu, J., Lu, G., . . . oth-  
 1029 ers (2018). Development and validation of the whole atmosphere community  
 1030 climate model with thermosphere and ionosphere extension (waccm-x 2.0).  
 1031 *Journal of Advances in Modeling Earth Systems*, 10(2), 381–402.
- 1032 Lockwood, M., & Cowley, S. (1992). Ionospheric convection and the substorm cy-  
 1033 cle. In: 'Substorms 1, Proceedings of the First International Conference on  
 1034 Substorms, ICS-1', 99–109.
- 1035 Lockwood, M., Hairston, M., Finch, I., & Rouillard, A. (2009). Transpolar voltage  
 1036 and polar cap flux during the substorm cycle and steady convection events.  
 1037 *Journal of Geophysical Research: Space Physics*, 114(A1).
- 1038 Lockwood, M., & McWilliams, K. A. (2021). On optimum solar wind-magnetosphere  
 1039 coupling functions for transpolar voltage and planetary geomagnetic activity.  
 1040 *Journal of Geophysical Research: Space Physics*, 126(12), e2021JA029946.

- 1041 Milan, S., Gosling, J., & Hubert, B. (2012). Relationship between interplanetary pa-  
 1042 rameters and the magnetopause reconnection rate quantified from observations  
 1043 of the expanding polar cap. *Journal of Geophysical Research: Space Physics*,  
 1044 *117*(A3).
- 1045 Milan, S., Provan, G., & Hubert, B. (2007). Magnetic flux transport in the dungey  
 1046 cycle: A survey of dayside and nightside reconnection rates. *Journal of Geo-  
 1047 physical Research: Space Physics*, *112*(A1).
- 1048 Pettigrew, E., Shepherd, S., & Ruohoniemi, J. (2010). Climatological patterns of  
 1049 high-latitude convection in the northern and southern hemispheres: Dipole  
 1050 tilt dependencies and interhemispheric comparisons. *Journal of Geophysical  
 1051 Research: Space Physics*, *115*(A7).
- 1052 Qian, L., Burns, A. G., Emery, B. A., Foster, B., Lu, G., Maute, A., ... Wang,  
 1053 W. (2014). The near tie-gcm: A community model of the coupled thermo-  
 1054 sphere/ionosphere system. *Modeling the ionosphere-thermosphere system*, *201*,  
 1055 73–83.
- 1056 Reiff, P., Spiro, R., Wolf, R., Kamide, Y., & King, J. (1985). Comparison of polar  
 1057 cap potential drops estimated from solar wind and ground magnetometer data:  
 1058 Cdaw 6. *Journal of Geophysical Research: Space Physics*, *90*(A2), 1318–1324.
- 1059 Reiff, P. H., Spiro, R. W., & Hill, T. (1981). Dependence of polar cap potential drop  
 1060 on interplanetary parameters. *Journal of Geophysical Research: Space Physics*,  
 1061 *86*(A9), 7639–7648.
- 1062 Rich, F., & Maynard, N. (1989). Consequences of using simple analytical functions  
 1063 for the high-latitude convection electric field. *Journal of Geophysical Research:  
 1064 Space Physics*, *94*(A4), 3687–3701.
- 1065 Richmond, A., & Kamide, Y. (1988). Mapping electrodynamic features of the  
 1066 high-latitude ionosphere from localized observations: Technique. *Journal of  
 1067 Geophysical Research: Space Physics*, *93*(A6), 5741–5759.
- 1068 Ridley, A., & Kihn, E. (2004). Polar cap index comparisons with amie cross polar  
 1069 cap potential, electric field, and polar cap area. *Geophysical research letters*,  
 1070 *31*(7).
- 1071 Ruohoniemi, J., & Baker, K. (1998). Large-scale imaging of high-latitude convection  
 1072 with super dual auroral radar network hf radar observations. *Journal of Geo-  
 1073 physical Research: Space Physics*, *103*(A9), 20797–20811.
- 1074 Ruohoniemi, J., & Greenwald, R. (1996). Statistical patterns of high-latitude con-  
 1075 vection obtained from goose bay hf radar observations. *Journal of Geophysical  
 1076 Research: Space Physics*, *101*(A10), 21743–21763.
- 1077 Shepherd, S. (2014). Altitude-adjusted corrected geomagnetic coordinates: Defi-  
 1078 nition and functional approximations. *Journal of Geophysical Research: Space  
 1079 Physics*, *119*(9), 7501–7521.
- 1080 Shepherd, S., Greenwald, R., & Ruohoniemi, J. (2002). Cross polar cap potentials  
 1081 measured with super dual auroral radar network during quasi-steady solar  
 1082 wind and interplanetary magnetic field conditions. *Journal of Geophysical  
 1083 Research: Space Physics*, *107*(A7), SMP–5.
- 1084 Shepherd, S. G. (2007). Polar cap potential saturation: Observations, theory, and  
 1085 modeling. *Journal of Atmospheric and Solar-Terrestrial Physics*, *69*(3), 234–  
 1086 248.
- 1087 Shue, J.-H., Chao, J., Fu, H., Russell, C., Song, P., Khurana, K., & Singer, H.  
 1088 (1997). A new functional form to study the solar wind control of the mag-  
 1089 netopause size and shape. *Journal of Geophysical Research: Space Physics*,  
 1090 *102*(A5), 9497–9511.
- 1091 Siscoe, G., & Huang, T. (1985). Polar cap inflation and deflation. *Journal of Geo-  
 1092 physical Research: Space Physics*, *90*(A1), 543–547.
- 1093 Siscoe, G. L. (1982). Polar cap size and potential: A predicted relationship. *Geo-  
 1094 physical Research Letters*, *9*(6), 672–675.
- 1095 SuperDARN Data Analysis Working Group, Schmidt, M., Bland, E., Thomas, E.,

- 1096 Burrell, A., Coco, I., . . . Walach, M.-T. (2021, August). *Superdarn/rst: Rst*  
 1097 *4.6*. Zenodo. Retrieved from <https://doi.org/10.5281/zenodo.5156752>  
 1098 doi: 10.5281/zenodo.5156752
- 1099 Thomas, E. G., & Shepherd, S. G. (2018). Statistical patterns of ionospheric con-  
 1100 vection derived from mid-latitude, high-latitude, and polar superdarn hf radar  
 1101 observations. *Journal of Geophysical Research: Space Physics*, *123*(4), 3196–  
 1102 3216.
- 1103 Volland, H. (1975). Models of the global electric fields within the magnetosphere.  
 1104 *Ann. Geophys.*, *31*, 159–173.
- 1105 Walach, M.-T., & Grocott, A. (2019). Superdarn observations during geomagnetic  
 1106 storms, geomagnetically active times, and enhanced solar wind driving. *Jour-*  
 1107 *nal of Geophysical Research: Space Physics*, *124*(7), 5828–5847.
- 1108 Walach, M.-T., & Grocott, A. (2022). Modelling the time-variability of the iono-  
 1109 spheric electric field (tivie). *Journal of Space Weather and Space Climate (Sub-*  
 1110 *mitted)*.
- 1111 Walach, M.-T., Grocott, A., & Milan, S. E. (2021). Average ionospheric electric  
 1112 field morphologies during geomagnetic storm phases. *Journal of Geophysical*  
 1113 *Research: Space Physics*, *126*(4), e2020JA028512.
- 1114 Walach, M.-T., Grocott, A., Staples, F., & Thomas, E. G. (2022). Super dual au-  
 1115 roral radar network expansion and its influence on the derived ionospheric  
 1116 convection pattern. *Journal of Geophysical Research: Space Physics*, *127*(2),  
 1117 e2021JA029559.
- 1118 Weimer, D. (1995). Models of high-latitude electric potentials derived with a least  
 1119 error fit of spherical harmonic coefficients. *Journal of Geophysical Research:*  
 1120 *Space Physics*, *100*(A10), 19595–19607.
- 1121 Weimer, D. (1996). A flexible, imf dependent model of high-latitude electric po-  
 1122 tentials having “space weather” applications. *Geophysical Research Letters*,  
 1123 *23*(18), 2549–2552.
- 1124 Weimer, D. (2001). An improved model of ionospheric electric potentials including  
 1125 substorm perturbations and application to the geospace environment modeling  
 1126 november 24, 1996, event. *Journal of Geophysical Research: Space Physics*,  
 1127 *106*(A1), 407–416.
- 1128 Weimer, D. (2005). Improved ionospheric electrodynamic models and application  
 1129 to calculating joule heating rates. *Journal of Geophysical Research: Space*  
 1130 *Physics*, *110*(A5).
- 1131 Weimer, D. (2019, January). *Weimer 2005 ionospheric electric potential model for*  
 1132 *IDL*. Zenodo. Retrieved from <https://doi.org/10.5281/zenodo.2530324>  
 1133 doi: 10.5281/zenodo.2530324

Figure 1.

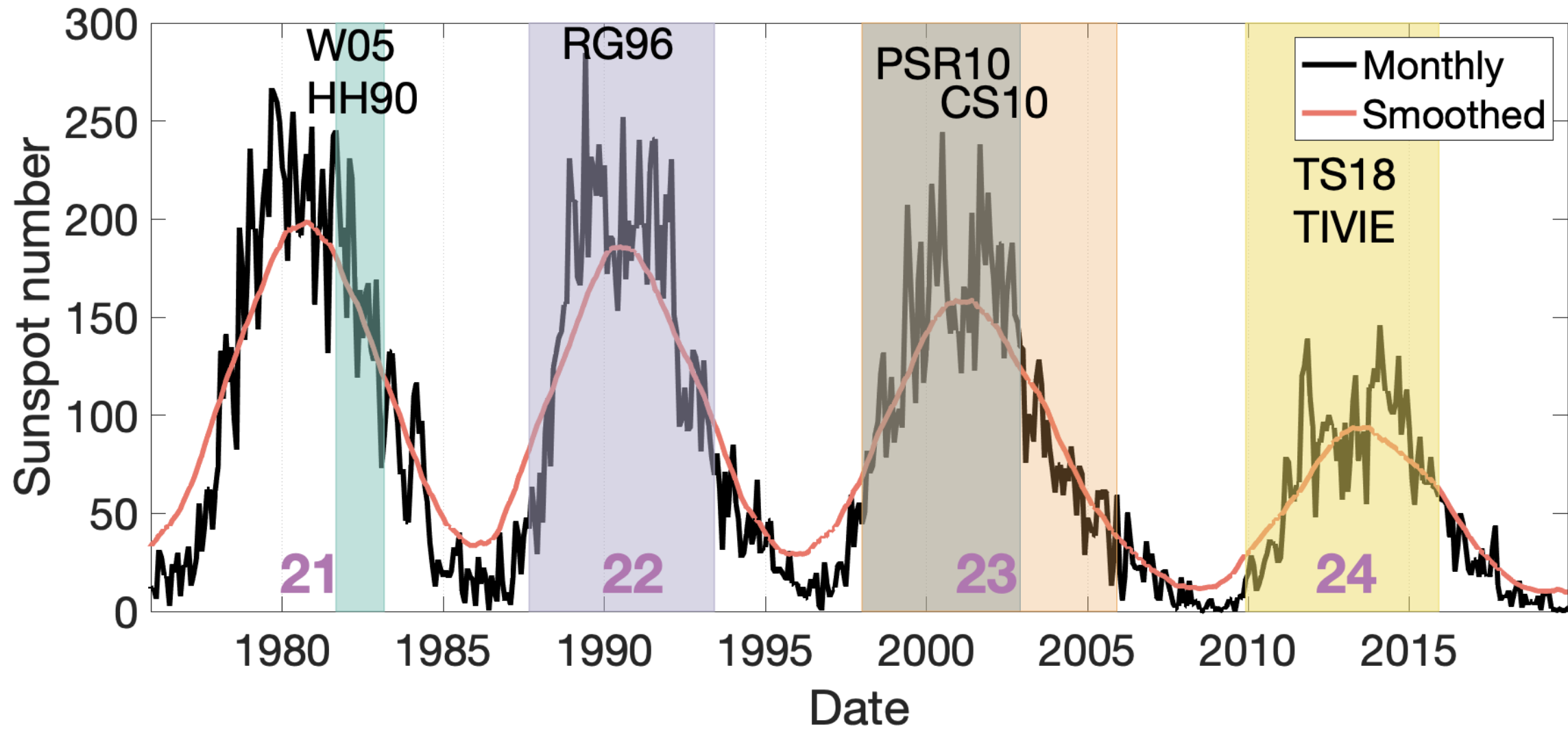


Figure 2.

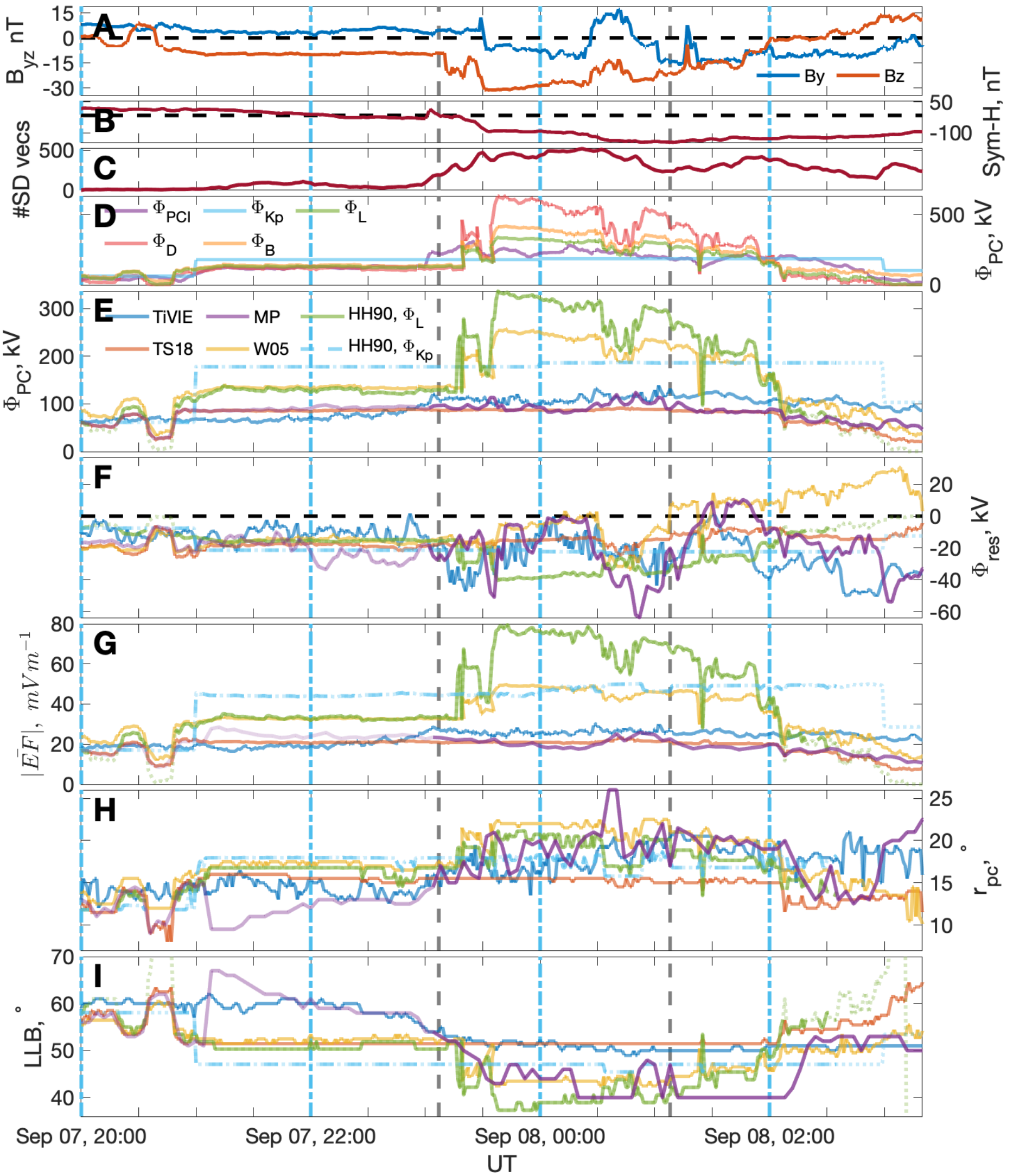


Figure 3.

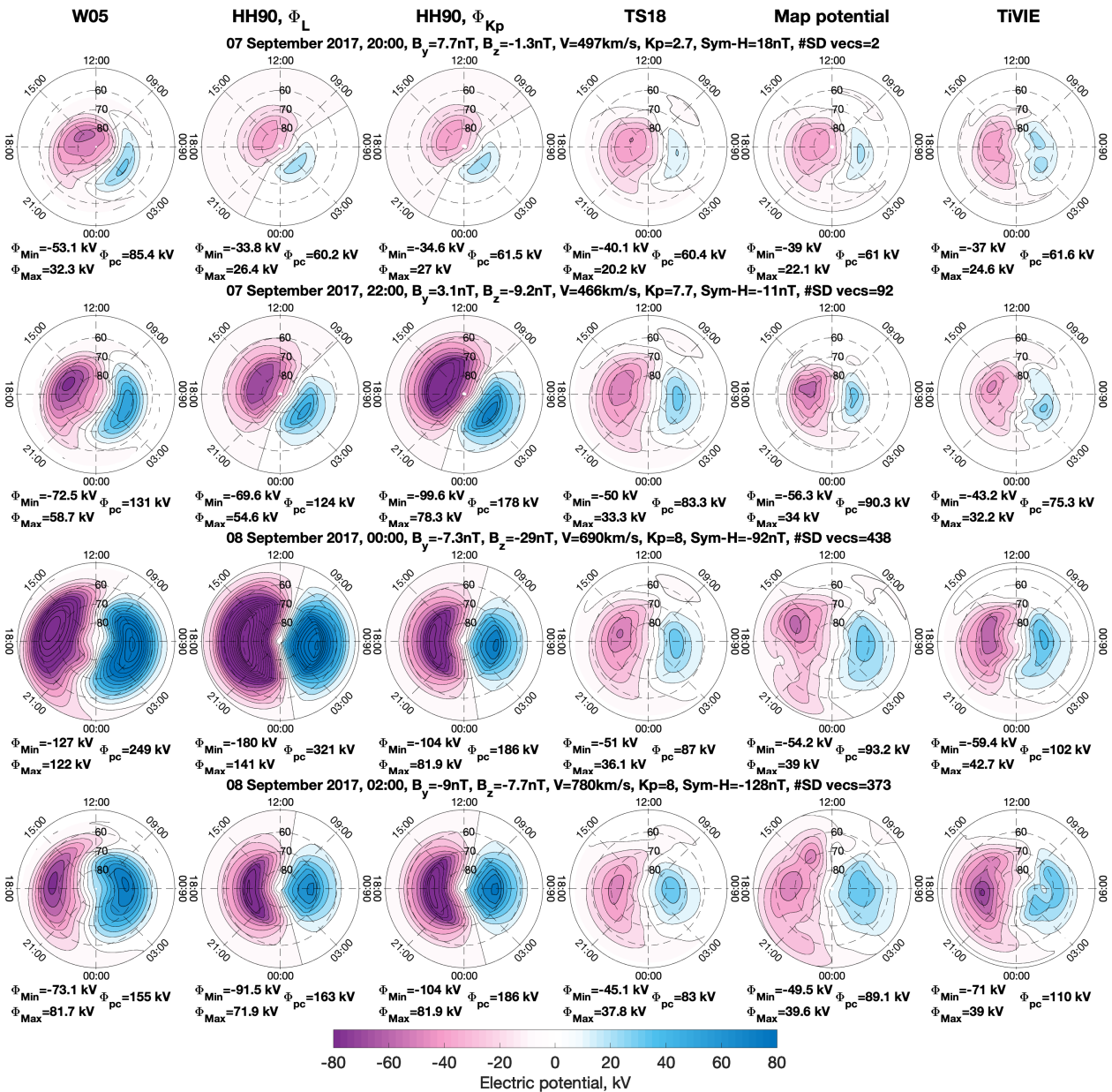
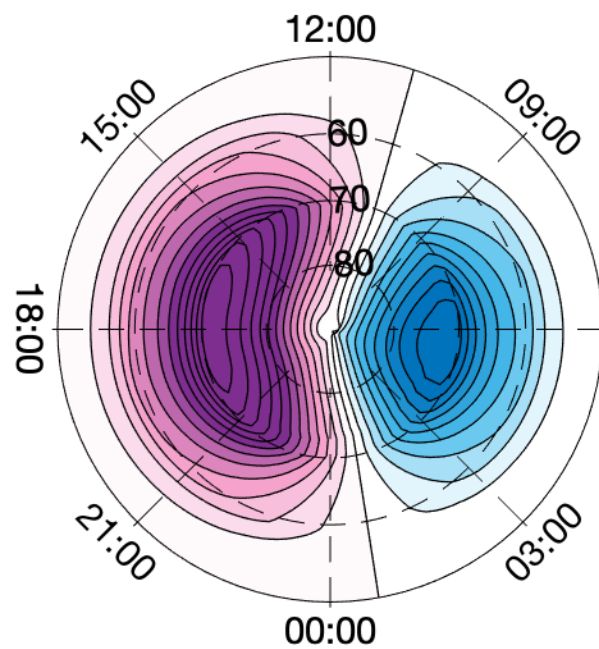
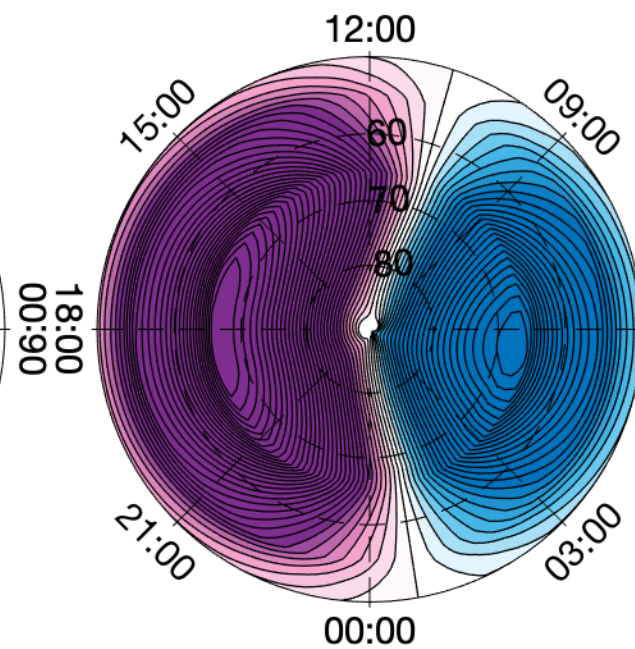


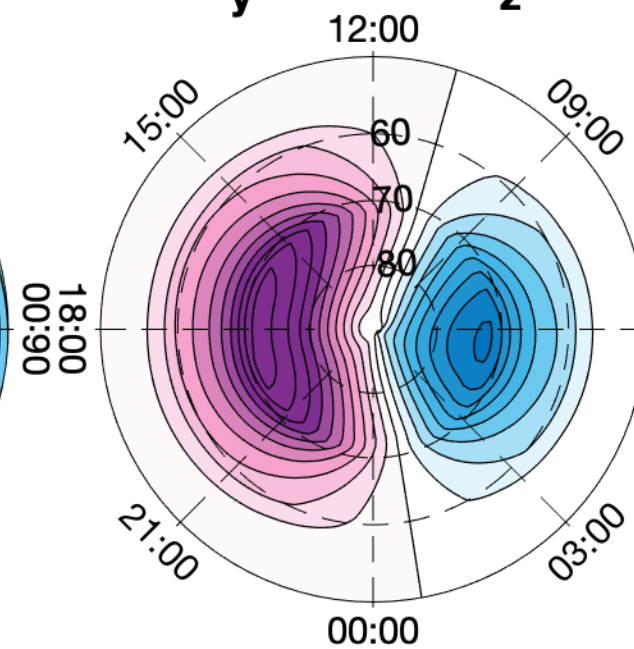
Figure 4.

a)  $\Phi_{\text{PCI}}$ 

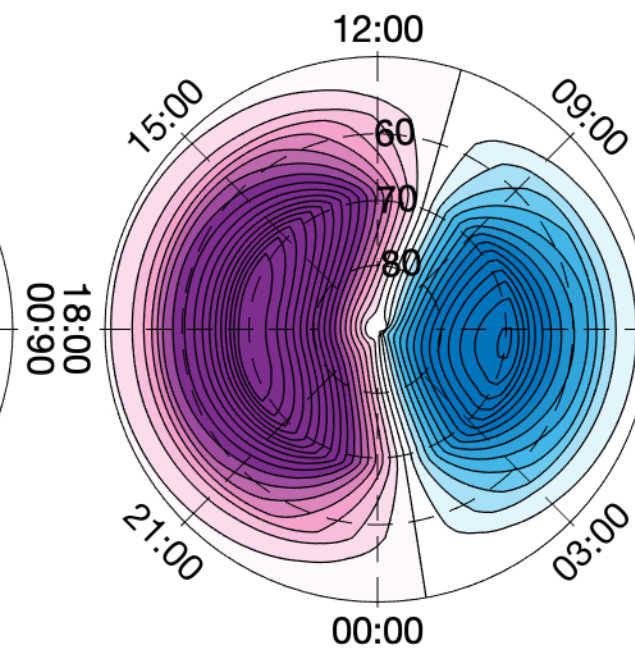
$\Phi_{\text{Min}} = -127 \text{ kV}$   $\Phi_{\text{pc}} = 226 \text{ kV}$   
 $\Phi_{\text{Max}} = 99.4 \text{ kV}$

b)  $\Phi_{\text{D}}$ 

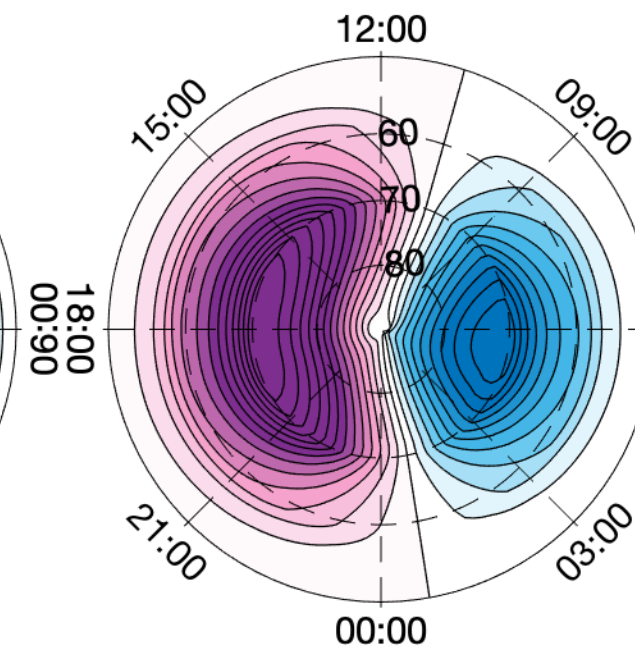
$\Phi_{\text{Min}} = -330 \text{ kV}$   $\Phi_{\text{pc}} = 589 \text{ kV}$   
 $\Phi_{\text{Max}} = 259 \text{ kV}$

c)  $\Phi_{\text{Kp}}$ 

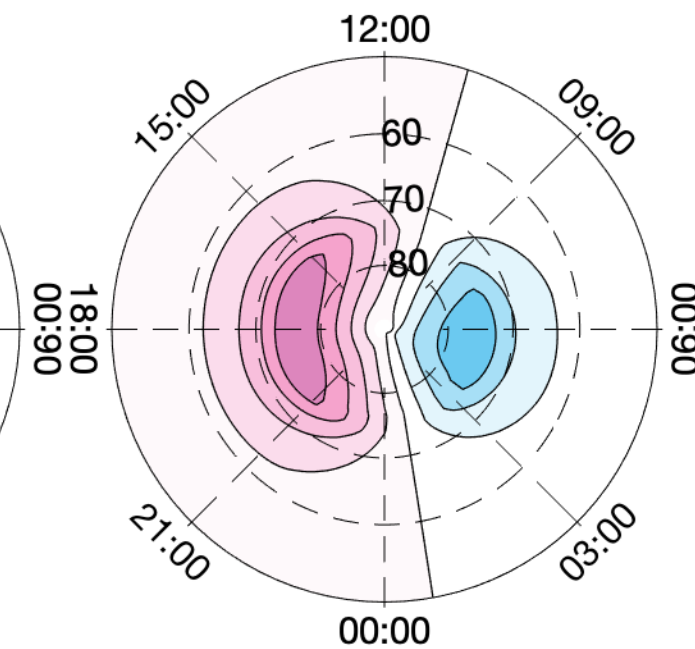
$\Phi_{\text{Min}} = -104 \text{ kV}$   $\Phi_{\text{pc}} = 186 \text{ kV}$   
 $\Phi_{\text{Max}} = 81.9 \text{ kV}$

d)  $\Phi_{\text{L}}$ 

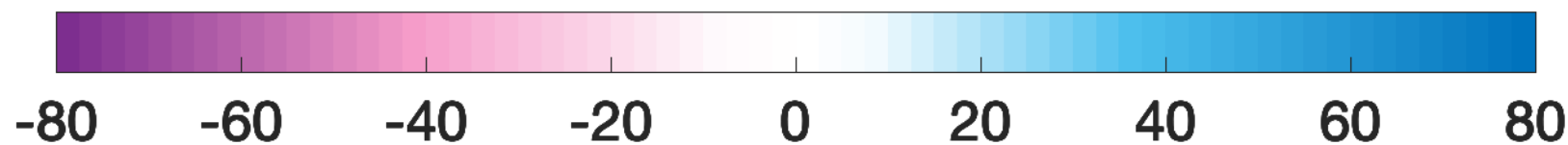
$\Phi_{\text{Min}} = -180 \text{ kV}$   $\Phi_{\text{pc}} = 321 \text{ kV}$   
 $\Phi_{\text{Max}} = 141 \text{ kV}$

e)  $\Phi_{\text{Weimer}}$ 

$\Phi_{\text{Min}} = -139 \text{ kV}$   $\Phi_{\text{pc}} = 249 \text{ kV}$   
 $\Phi_{\text{Max}} = 110 \text{ kV}$

f)  $\Phi_{\text{TS18}}$ 

$\Phi_{\text{Min}} = -48.7 \text{ kV}$   $\Phi_{\text{pc}} = 86.9 \text{ kV}$   
 $\Phi_{\text{Max}} = 38.3 \text{ kV}$



Electric potential, kV

08 September 2017, 00:00,  $B_y = -7.3 \text{ nT}$ ,  $B_z = -29 \text{ nT}$ ,  $V = 690 \text{ km/s}$ ,  $K_p = 8$ ,  $\text{SYM/H} = -92 \text{ nT}$ ,  $\text{\#vecs} = 219$

Figure 5.

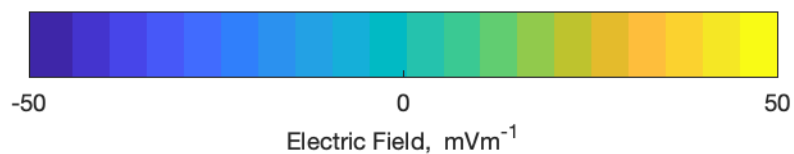
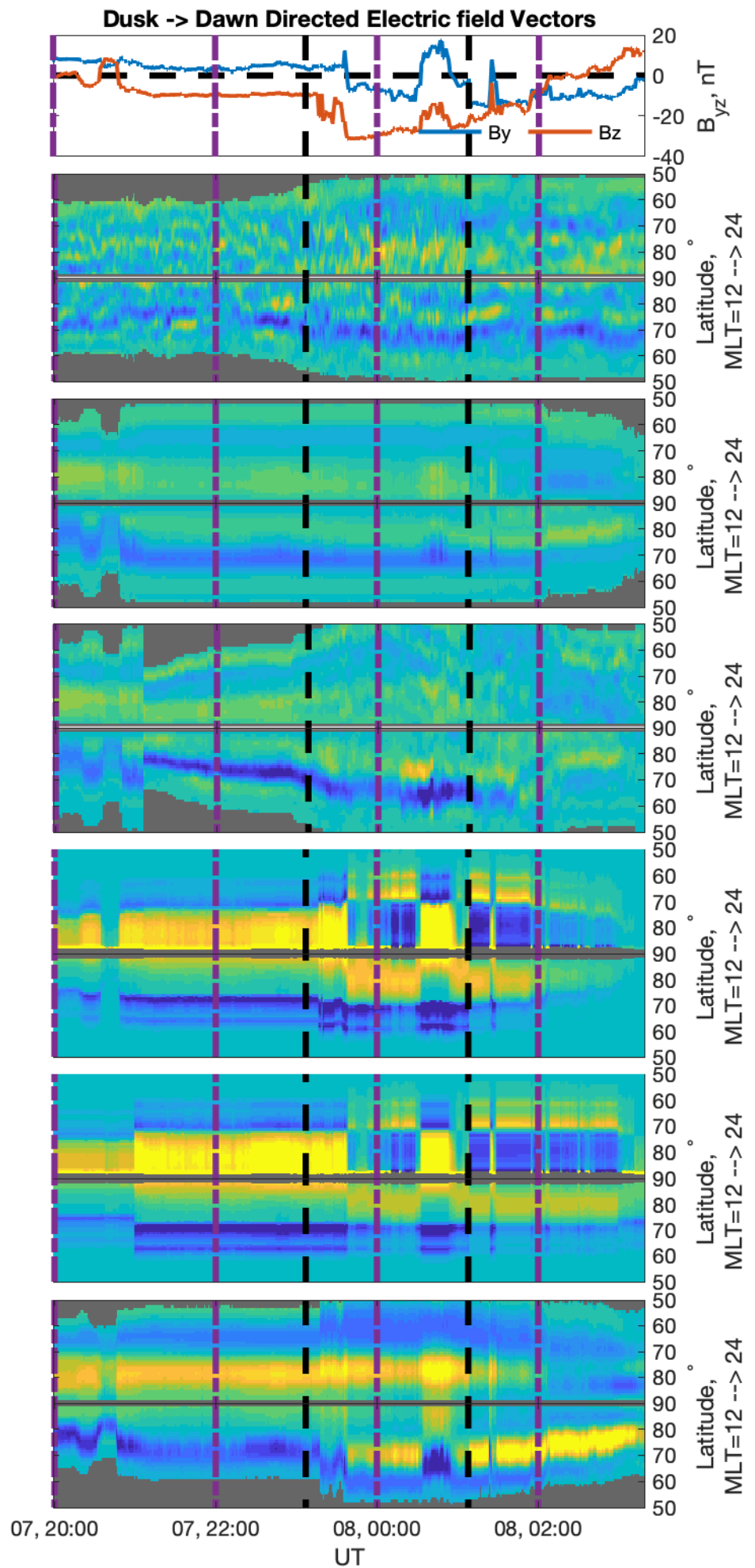
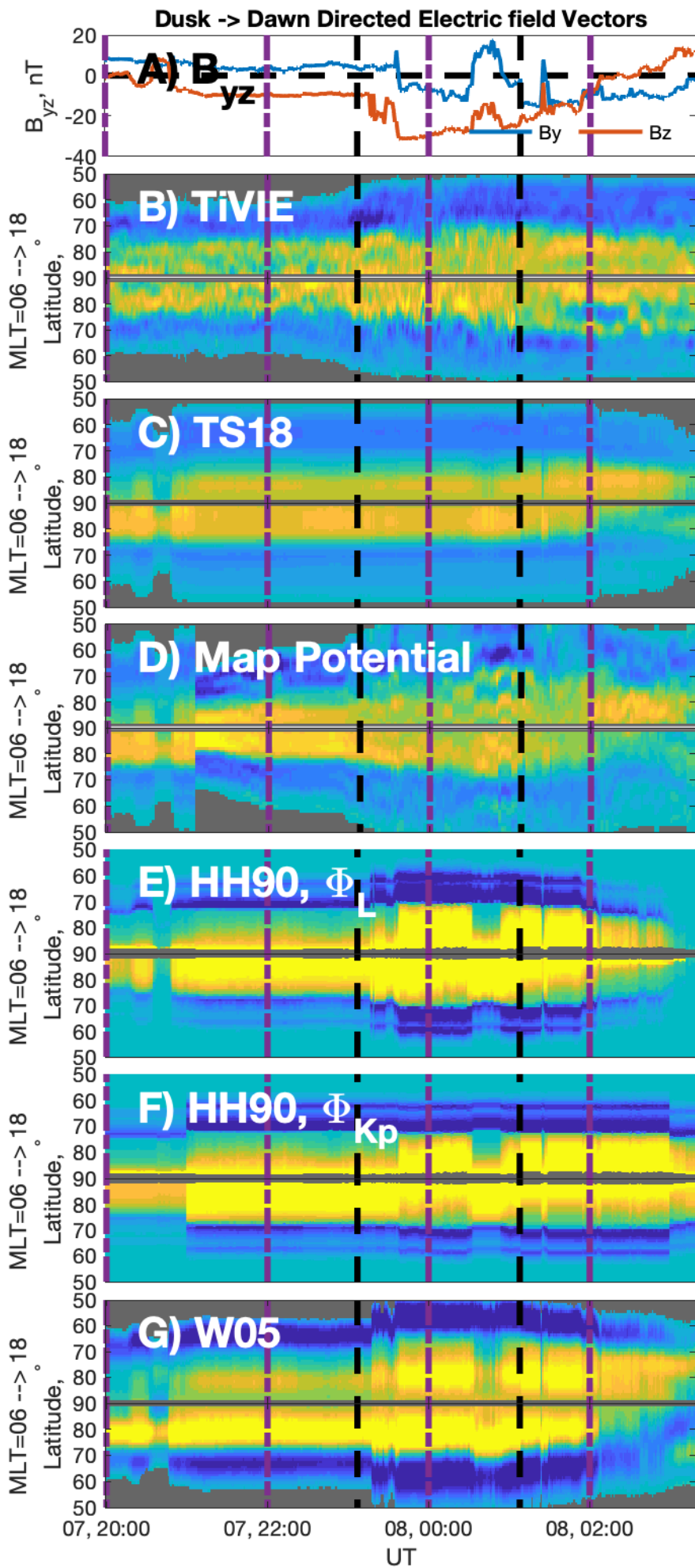


Figure 6.

# $\Phi_{PC}$ , kV

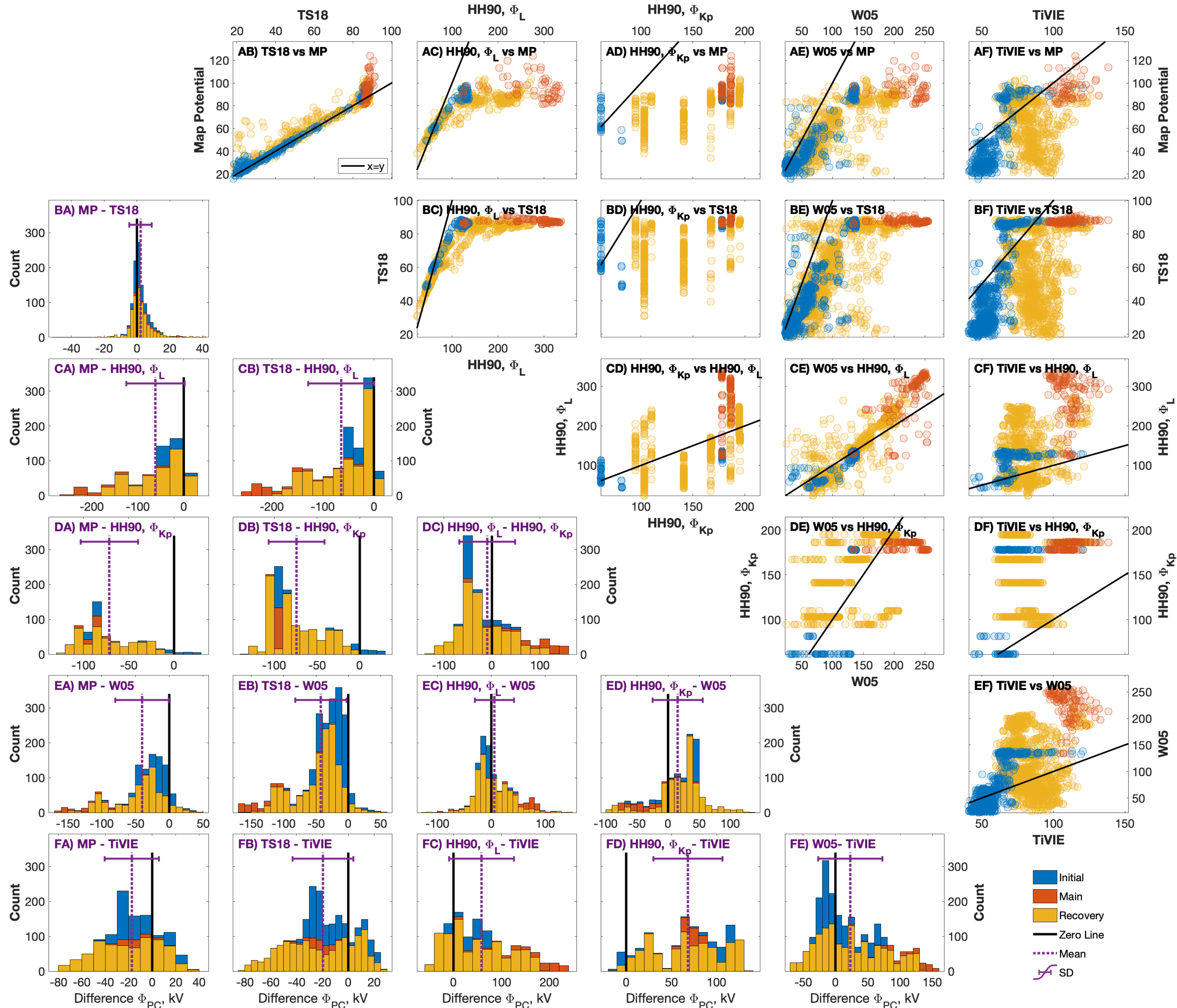
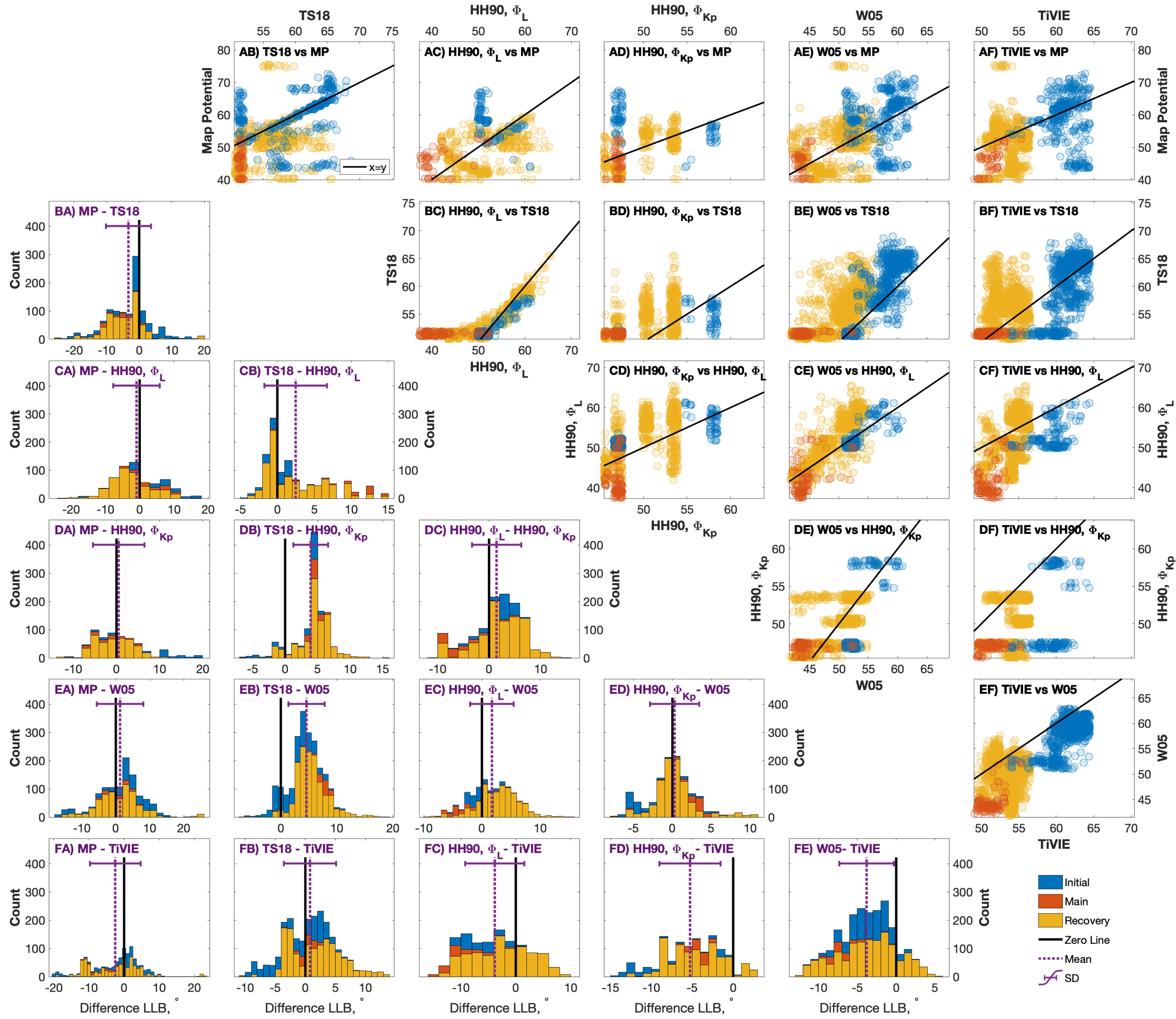


Figure 7.

LLB, °



# Supporting Information for ”A quantitative comparison of high latitude electric field models during a large geomagnetic storm”

L. Orr<sup>1</sup>, A. Grocott<sup>1</sup>, M.-T. Walach<sup>1</sup>, G. Chisham<sup>2</sup>, M.P. Freeman<sup>2</sup>, M.M.

Lam<sup>2</sup>, R.M. Shore<sup>2</sup>

<sup>1</sup>Space and Planetary Physics, Lancaster University

<sup>2</sup>British Antarctic Survey

## Contents of this file

1. Description of the AENeAS version of the Heelis model code
2. Figures S1 to S7

---

## 1. AENeAS version of Heelis code

The TIE GCM version of Heelis (used within AENeAS (?, ?)) uses similar equations to those defined in (Hairston & Heelis, 1990). It is parameterised using  $B_y$  (nT) and cross polar cap potential,  $\Phi_{cp}$  (kV). IMF  $B_y$  is set to be in the range  $-11 \leq B_y \leq 7$  in the northern hemisphere and  $-7 \leq B_y \leq 11$  in the southern hemisphere. TIE GCM uses an expression of Kp to represent the cross polar cap potential.

$$\Psi_{cp} = 15 + 15Kp + 0.8Kp^2. \quad (1)$$

### 1.1. Initial equations

The center (origin) of the polar cap circle is offset from the geomagnetic poles by  $offc$  along the magnetic noon-midnight line and  $D_c$  in the dawn-dusk direction. N.B. equations given in degrees are converted to radians in the TIE GCM code. The plus and minus ( $\pm$ ) refers to the northern and southern hemisphere, respectively.

$$Offc = 1.1^\circ, \quad \text{Offset of convection towards 0 MLT relative to magnetic pole.} \quad (2)$$

$$D_c = -0.08^\circ \pm 0.15B_y^\circ, \quad \text{Offset of convection in radians towards 18 MLT.} \quad (3)$$

The parameter,  $r$ , describes the decay of the potential equatorward of the convection reversal boundary, (Hairston & Heelis, 1990). It is set to the value of -2.6 in TIE GCM from average AMIE results.

$$r = -2.6, \quad \text{Exponential fall-off of convection from convection radius.} \quad (4)$$

The convection flow reversal circle,  $\theta_0$ , is similar to equation 1 in Hairston and Heelis (1990) and that defined in Siscoe (1982).

$$\theta_0 = -3.8^\circ + 8.48^\circ \Psi_{pc}^{0.1875}, \quad \text{Convection reversal boundary.} \quad (5)$$

The potential at the maximum, minimum and centre of the convection pattern ( $\psi_m$ ,  $\psi_e$  and  $\Psi_0$  respectively. These equations are of the same form as equations in Hairston and Heelis (1990) but have different values (? , ?).

$$\psi_m = 0.44 \Psi_{pc} \times 1000 = \psi_3 = \psi_4 = \psi_7 = \psi_8, \quad \text{Maximum potential in morning cell,} \quad (6)$$

$$\psi_e = -0.56 \Psi_{pc} \times 1000 = \psi_1 = \psi_2 = \psi_5 = \psi_6, \quad \text{Minimum potential in evening cell.} \quad (7)$$

$$\Psi_0 = (-0.168 \mp 0.027 B_y) \Psi_{pc} \times 1000, \quad \text{Potential at the centre.} \quad (8)$$

The dayside and nightside convection entrance, or zero potential line,  $\phi_d$  and  $\phi_n$ , are first defined in MLT such that  $\phi = 0$  is noon, before converting to degree and then to radians. The local magnetic time dependencies are described by six angles, similar to those described in Heelis, Lowell, and Spiro (1982). The maximum locations are the minimum of  $\pi/2$  or half way between the dayside and nightside zero potential lines.

$$\phi_d = (9.39 \mp 0.21 B_y - 12) 15^\circ, \quad \text{Dayside convection entrance} \quad (9)$$

$$\phi_n = (23.50 \mp 0.15 B_y - 12) 15^\circ, \quad \text{Nightside convection entrance} \quad (10)$$

$$\phi_{dp}^{mx} = \frac{1}{2} \min(\pi, \phi_n - \phi_d), \quad (11)$$

$$\phi_{np}^{mx} = \frac{1}{2} \min(\pi, \phi_d - \phi_n + 2\pi), \quad (12)$$

$$\phi_{nm}^{mx} = \phi_{dp}^{mx}, \quad (13)$$

$$\phi_{dm}^{mx} = \phi_{np}^{mx}. \quad (14)$$

## 1.2. Magnetic latitude and longitude

If  $nlt$  is the number of latitude points,  $1 \leq \mathbf{lt} \leq nlt$ . The resulting magnetic latitude  $\theta_m$  is not equally spaced.

$$r0 = 6.37122e8 + 9.0e6, \quad (15)$$

$$r1 = 1.06e7, \quad (16)$$

$$\theta_N = (\mathbf{lt} - 1) \left( \frac{\pi}{nlt} \right) - \frac{\pi}{2}, \quad (17)$$

$$\mathbf{hamh0} = r1 |\tan \theta_N| + r0 \frac{|\tan \theta_N|^{(2+2 \times 1.668)}}{(1 + |\tan \theta_N|^2)^{1.668}}, \quad (18)$$

$$\theta_m = \mathbf{ylatm} = \left\{ \arctan \left( \frac{\mathbf{hamh0}}{r0} \right)^{\frac{1}{2}}, \text{ if } \theta_N > 0, -\arctan \left( \frac{\mathbf{hamh0}}{r0} \right)^{\frac{1}{2}}, \text{ if } \theta_N < 0. \right. \quad (19)$$

Poles are equal to  $\theta_N([\mathbf{1}, \mathbf{nlt}])$ .

$nlon$  is the number of longitude points,  $\mathbf{lon}$  is 1 to  $nlon$ .  $\mathbf{Sunlons}$  defines the Sun's longitude in dipole coordinates from date.

$$\phi_m = \mathbf{ylonm} = \frac{2\pi(\mathbf{lon} - 1)}{nlon} - \pi - \mathbf{sunlons}. \quad (20)$$

### 1.2.1. Auroral Circle Coordinates

$$O_c = (O_{ffc}^2 + D_C^2)^{\frac{1}{2}}, \quad (21)$$

$$\phi_{off} = \mathbf{aslonc} = \arcsin \frac{D_c}{O_c}, \quad (22)$$

$$\theta = \mathbf{colat} = \arccos (\cos O_c \sin |\theta_m| - \sin O_c \cos \theta_m \cos (\phi_m + \phi_{off})), \quad (23)$$

$$\phi_a = \mathbf{alon} = (\mathbf{A}, 2\pi) - \pi, \quad (24)$$

where  $\mathbf{A} = \arctan 2(\mathbf{X}, \mathbf{Y}) - \phi_{off} + 3\pi$ ,  $\mathbf{X} = \sin (\phi_m + \phi_{off}) \cos \theta_m$ , and  $\mathbf{Y} = \sin |\theta_m| \sin O_c + \cos O_c \cos \theta_m \cos (\phi_m + \phi_{off})$ .

### 1.2.2. Boundaries for longitudinal function:

$$\phi_4 = \phi_d + 10^{-6} - \min\left(\frac{\pi}{2}, \phi_{dm}^{mx}\right), \quad (25)$$

$$\phi_5 = \phi_d - 10^{-6} + \min\left(\frac{\pi}{2}, \phi_{dp}^{mx}\right), \quad (26)$$

$$\phi_6 = \phi_n + 10^{-6} - \min\left(\frac{\pi}{2}, \phi_{nm}^{mx}\right), \quad (27)$$

$$\phi_7 = \phi_n - 10^{-6} + \min\left(\frac{\pi}{2}, \phi_{np}^{mx}\right), \quad (28)$$

$$\phi_1 = \phi_5 - 2\pi, \quad (29)$$

$$\phi_2 = \phi_6 - 2\pi, \quad (30)$$

$$\phi_3 = \phi_7 - 2\pi, \quad (31)$$

$$\phi_8 = \phi_4 + 2\pi. \quad (32)$$

### 1.2.3. Ring current rotation to potential

TIE GCM is set to have no ring current rotation hence:

$$\mathbf{wk}_2 = (\phi_a + 5\pi, 2\pi) - \pi, \quad (33)$$

$$\mathbf{wk}_3 = (\phi_a + 6\pi, 2\pi) - \pi. \quad (34)$$

### 1.3. Longitudinal variation:

$$\Psi_{\text{fun}} = \Psi_{\text{fn}2} = 0 \quad (35)$$

For  $n = 1$  to  $7$

$$\Psi_{\text{fun}} = \Psi_{\text{fun}} + \frac{1}{4} \left( \psi_n + \psi_{n+1} + (\psi_n - \psi_{n+1}) \cos\left(\frac{\pi(\mathbf{wk}_2 - \phi_n)}{\phi_{n+1} - \phi_n}\right) \right), \quad (36)$$

if  $(\mathbf{wk}_2 - \phi_n)(\mathbf{wk}_2 - \phi_{n+1}) < 0$ , or  $\Psi_{\text{fun}} = \Psi_{\text{fun}}$  if  $(\mathbf{wk}_2 - \phi_n)(\mathbf{wk}_2 - \phi_{n+1}) > 0$ .

And

$$\Psi_{\text{fn2}} = \Psi_{\text{fn2}} + \frac{1}{4} \left( \psi_n + \psi_{n+1} + (\psi_n - \psi_{n+1}) \cos \left( \frac{\pi(\mathbf{wk}_3 - \phi_n)}{\phi_{n+1} - \phi_n} \right) \right), \quad (37)$$

if  $(\mathbf{wk}_3 - \phi_n)(\mathbf{wk}_3 - \phi_{n+1}) < 0$  or  $\Psi_{\text{fn2}} = \Psi_{\text{fn2}}$  if  $(\mathbf{wk}_3 - \phi_n)(\mathbf{wk}_3 - \phi_{n+1}) > 0$ .

#### 1.4. Evaluate total potential:

Equations for the total potential are given below. Equation 38 gives the potential inside the polar cap and is the same as equation 4 provided in (Hairston & Heelis, 1990). Equation 39 is quite different from the trigonometric or Gaussian functions suggested as frequent expressions of the latitudinal distribution outside of the cap by (Hairston & Heelis, 1990).

Inside the polar cap:

$$\Psi_{\text{tot}} = A \left( \frac{\theta}{\theta_0} \right)^3 + B \left( \frac{\theta}{\theta_0} \right)^2 + C \left( \frac{\theta}{\theta_0} \right) + \Psi_0, \quad (38)$$

where  $A = \left( 2(\Psi_0 - \Psi_{\text{fun}}) + \frac{3}{4}(\Psi_{\text{fun}} - \Psi_{\text{fn2}}) \right)$ ,  $B = 3 \left( \frac{1}{2}(\Psi_{\text{fun}} + \Psi_{\text{fn2}}) - \Psi_0 \right)$  and  $C = \frac{3}{4}(\Psi_{\text{fun}} - \Psi_{\text{fn2}})$ .

Outside the polar cap:

$$\Psi_{\text{tot}} = \Psi_{\text{fun}} \left( \frac{\max(\sin \theta, \sin \theta_0)}{\sin \theta_0} \right)^r \times \exp \left( 7 \left( 1 - \frac{\max(\sin \theta, \sin(\theta_0 + 0.1972))}{\sin(\theta_0 + 0.1972)} \right) \right). \quad (39)$$

Average amie results show  $r1 = -2.6$  for 11.3 degrees (0.1972 rad) beyond  $\theta_0$ .

## Figures S1 to S7

### References

- Hairston, M., & Heelis, R. (1990). Model of the high-latitude ionospheric convection pattern during southward interplanetary magnetic field using de 2 data. *Journal of Geophysical Research: Space Physics*, *95*(A3), 2333–2343.
- Heelis, R., Lowell, J. K., & Spiro, R. W. (1982). A model of the high-latitude ionospheric convection pattern. *Journal of Geophysical Research: Space Physics*, *87*(A8), 6339–6345.
- Siscoe, G. L. (1982). Polar cap size and potential: A predicted relationship. *Geophysical Research Letters*, *9*(6), 672–675.

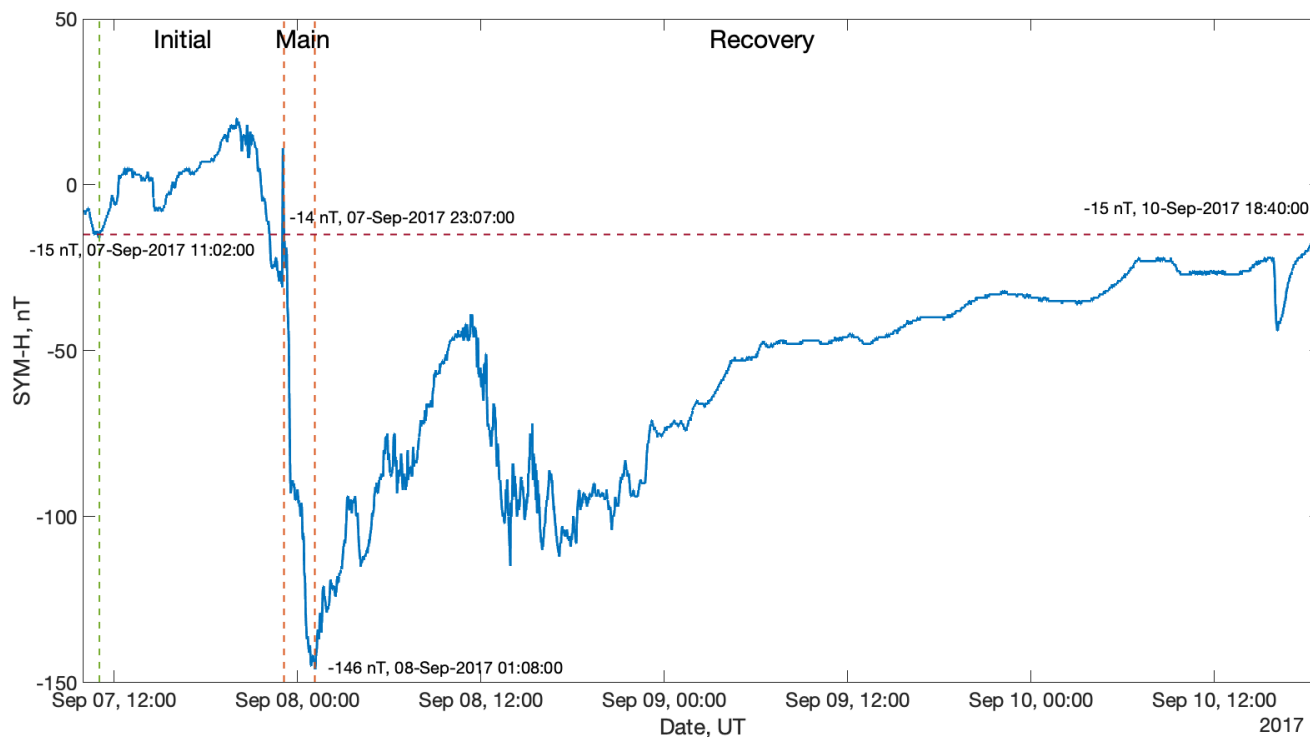


**Figure S1.** Sym-H for timings associated with TiVIE mode 3

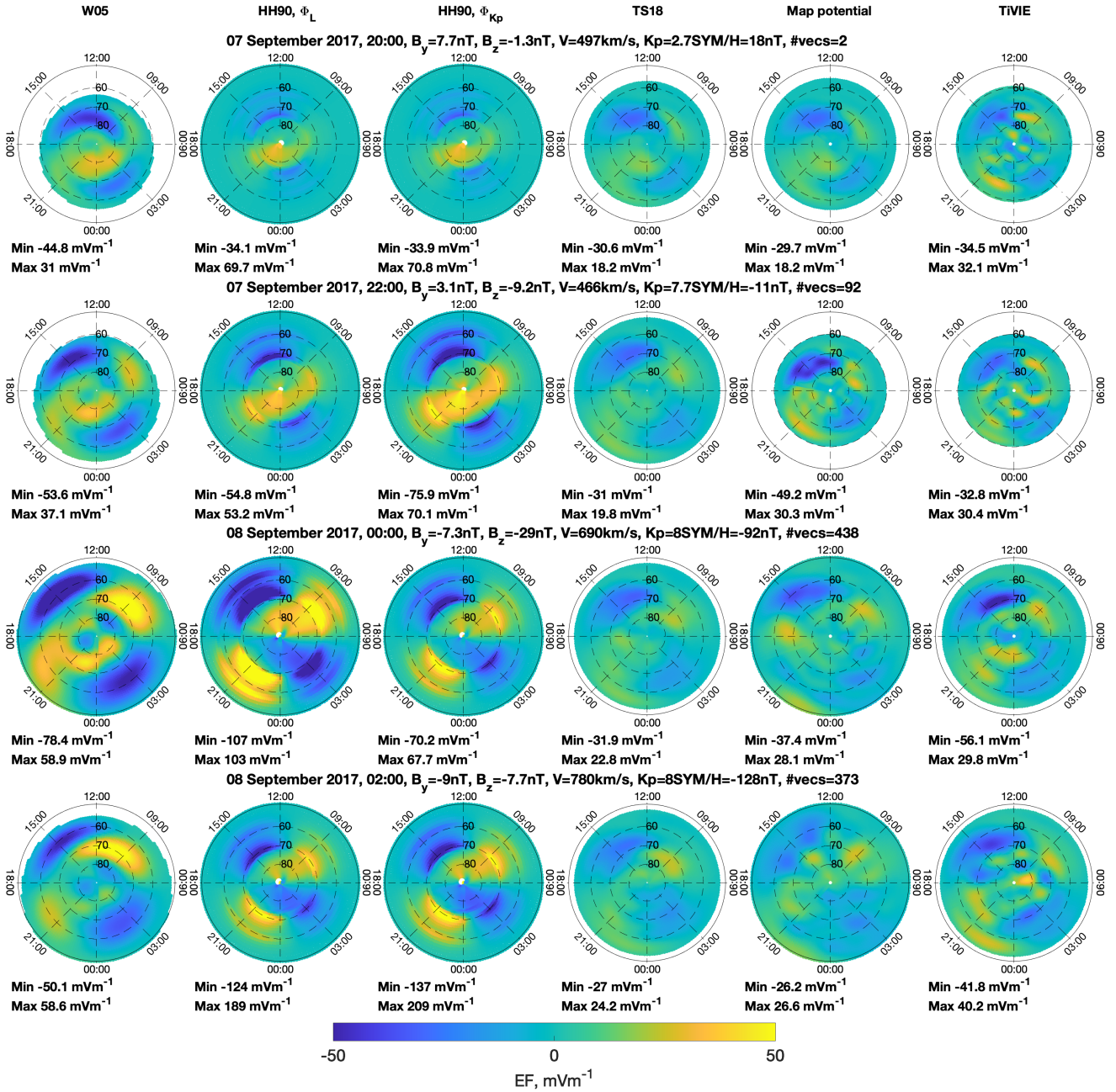


**Figure S2.** Midnight-to-noon directed component of the electric field vector in magnetic coordinates for the five models are four time intervals. Yellow represents positive, Midnight-to-noon directed electric field and blue negative, noon-to-midnight directed as shown in the colour bar. A selection of parameters including the time, IMF conditions, SW velocity,  $K_p$ , Sym/H and the number of SuperDARN vectors are provided per panel.

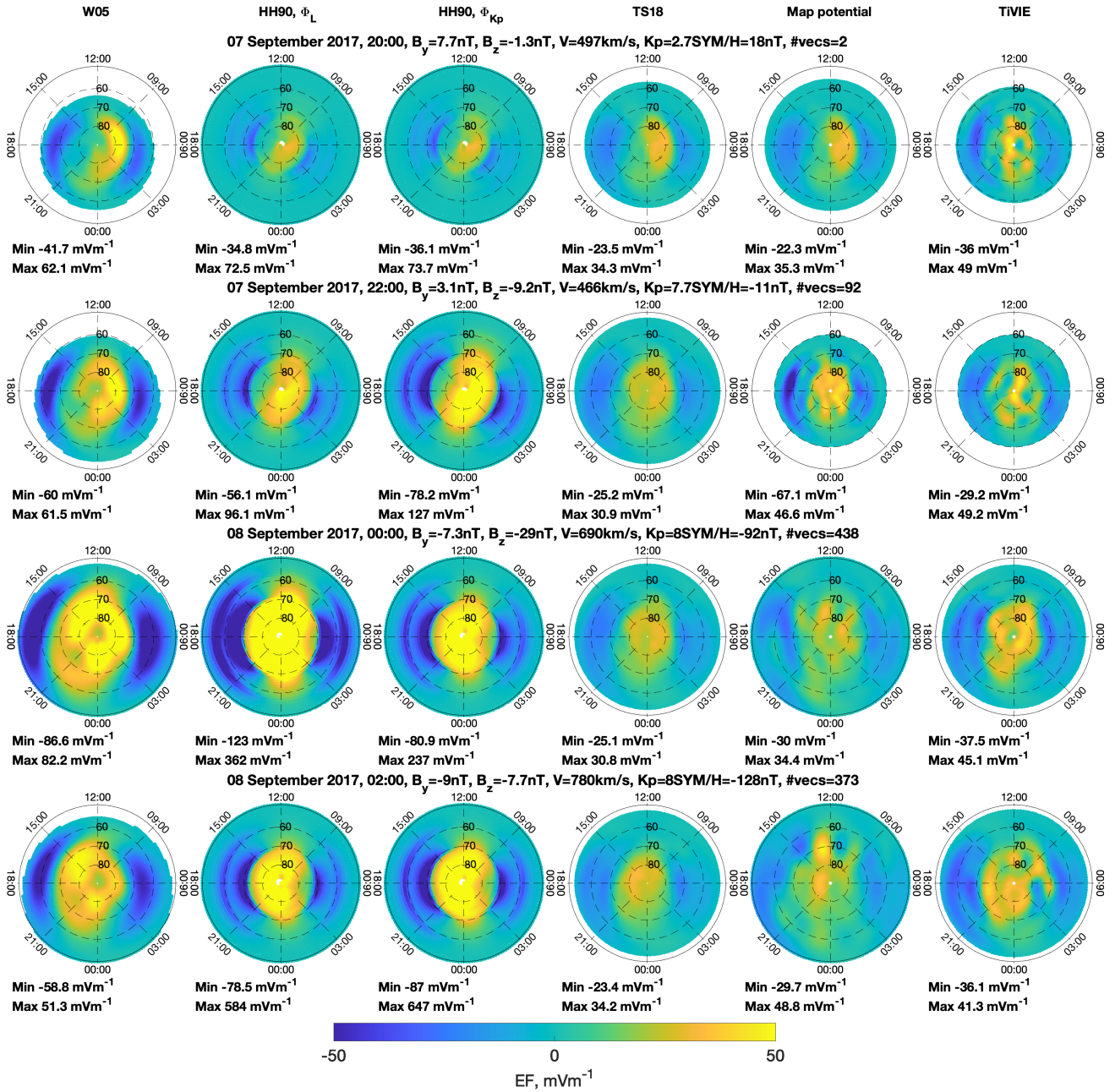


**Figure S3.** Dawn-to-dusk directed component of the electric field vector in magnetic coordinates for the five models are four time intervals. Yellow represents positive, Dawn-to-dusk electric field and blue negative, dusk-to-dawn directed as shown in the colour bar. A selection of parameters including the time, IMF conditions, SW velocity, Kp, Sym/H and the number of SuperDARN vectors are provided per panel.

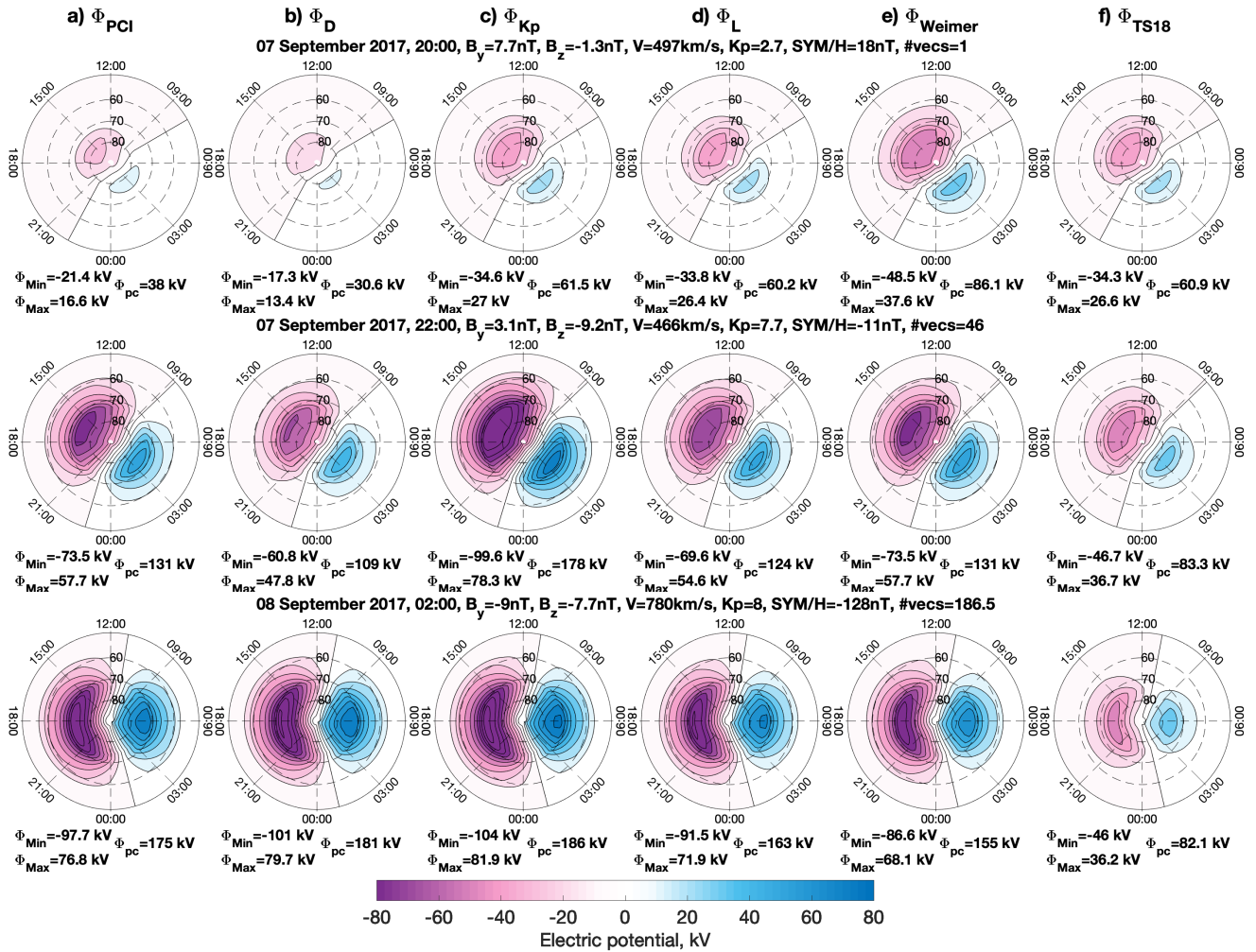


**Figure S4.** Convection maps in magnetic coordinates with contour lines representing 10kV intervals for the heelis model with six  $\Phi_{PC}$  proxies are four time intervals. Purple/pink represents negative electric potential and blue positive, as shown in the colour bar. A selection of parameters including the time, IMF conditions, SW velocity, Kp, Sym/H and the number of SuperDARN vectors are provided per panel.

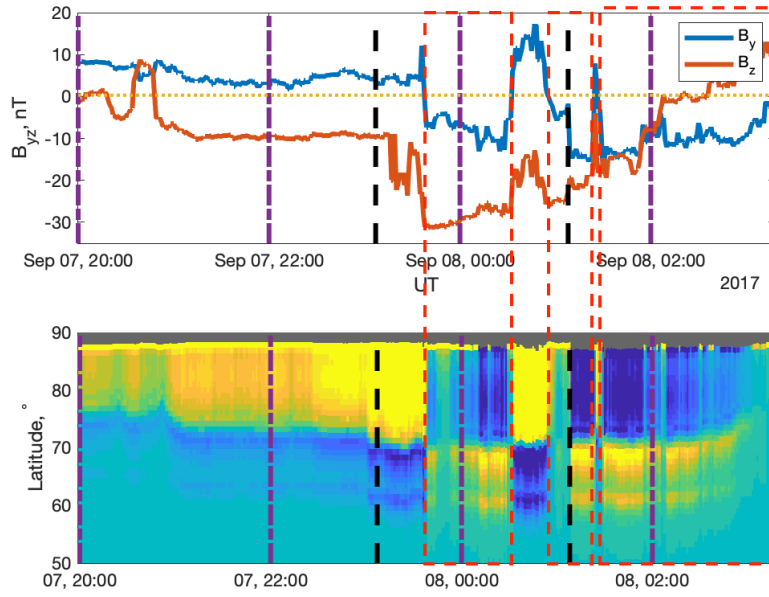


**Figure S5.** Figure highlighting the effect of the  $B_y$  component on the electric field north-south component from the Heelis model at midnight. A zoomed in version of figure 4, main text.

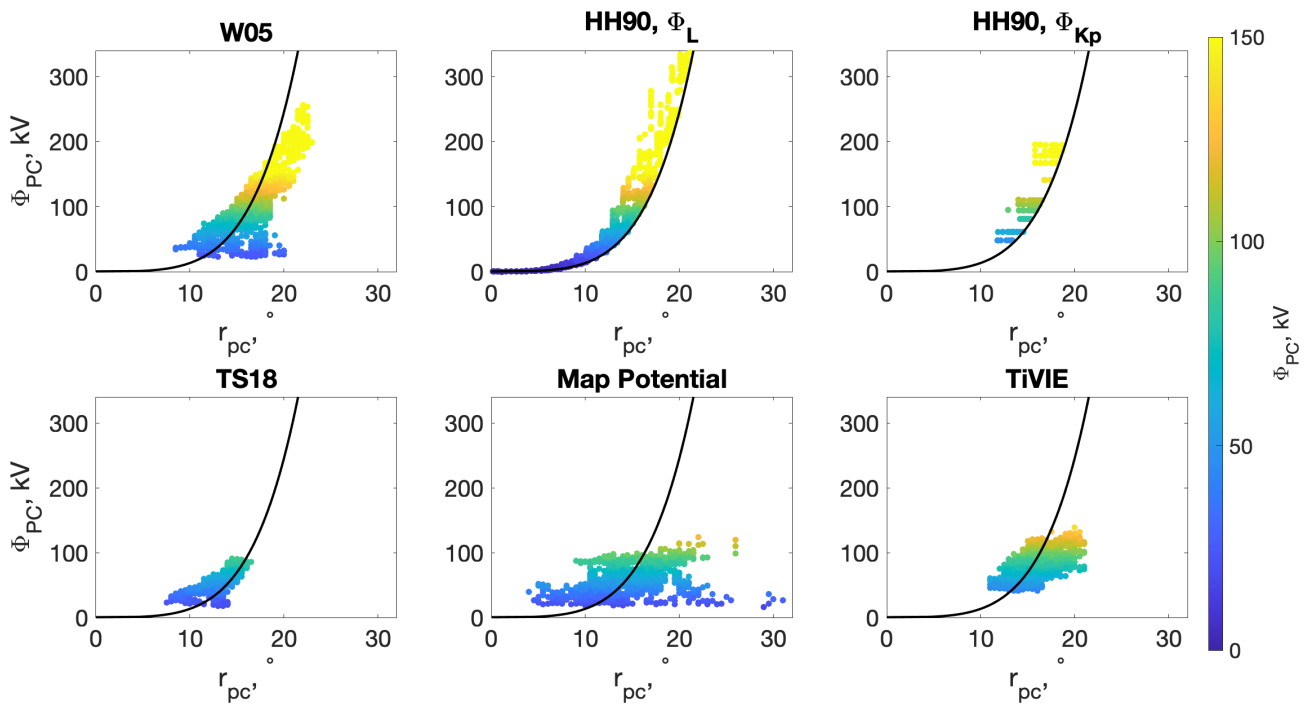


**Figure S6.** Proxy for the size of the polar cap,  $r_{pc}$  vs the cross polar cap potential,  $\Phi_{PC}$ . The black line shows the trend the Heelis model uses for the convection reversal boundary.

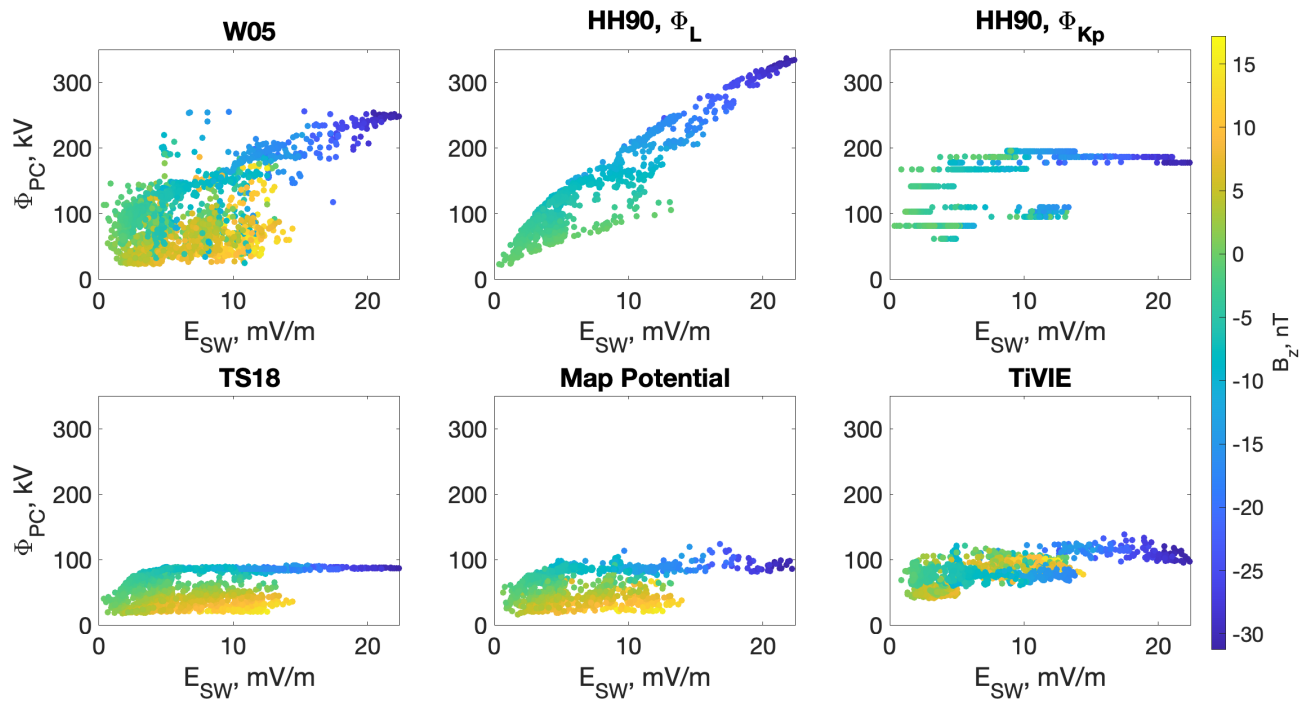


**Figure S7.** Scatter plot of  $E_{SW}$  vs  $\Phi_{PC}$  with the colour representing  $B_z$ .